Analysis of Interstellar Cloud Properties With Laplacian Pyramid Transforms: 1. IRAS Maps

William D. Langer[1], Charles H. Anderson[2], and Robert W. Wilson[3,4]

1. Jet Propulsion Laboratory, California Institute of Technology, MS 169-506, Pasadena, CA 91109.
2. Washington University School of Medicine, St. Louis, MO 63110.
3. AT&T Bell Laboratories, Holmdel, NJ 07733.
4. Center for Astrophysics, 60 Garden Street, Cambridge,MA02138 (current address).

e-mail: langer@langer.jpl.nasa.gov

Submitted to *The Astrophysical Journal.*

ABSTRACT

We analyze the properties of IRAS maps of interstellar clouds using Laplacian Pyramid Transforms, a member of the class of transforms with multiscale properties. Multiscale transforms provide a means to decompose images into their spatial frequency components such that all spatial scales are treated in an equivalent manner. The Laplacian Pyramid Transform has a number of advantages over traditional orthogonal wavelets for analyzing the properties of astronomical maps. Here we use this transform to analyze the properties of IRAS 100 µm maps of dust emission from clouds in the North Polar and Chameleon regions. We derive their space-scale energy density, global energy (power) spectrum, and intermittency. We also develop a set of map measures based on statistical distributions of the properties of the fluctuations in the Laplacian maps. Such measures are necessary to characterize large scale astronomical maps and to connect the map measures to physical properties. All the image analysis reported here was done with a program we developed called Astrophysics Pyramid image Processing, or APIP for short. The global energy spectrum shows systematic differences among interstellar clouds depending on the degree of evolution towards higher density structures. We identify the fluctuations in the cloud structure by separating all connected zero boundary regions in the Laplacian maps. The statistical properties of these fluctuations are used to characterize the maps. These structures are also analyzed with respect to their Hausdorff dimension for evidence of the scaling relationships in these clouds. We find that the structures within the maps are multi-fractal having different scaling relationships with size. The spatial scaling of the features span the range from regular objects to filaments having both linear and web-like structures, and including all fractal scalings in between. The lack of a single scaling law is consistent with different forces driving the cloud evolution and fragmentation on different length scales.

Subject headings: methods: data analysis -- ISM: interstellar clouds -- ISM: individual: Chameleon, North Polar Region

1. INTRODUCTION

interstellar clouds are inhomogeneous on almost all scales and this inhomogeneity results from a complex dynamical process whose mechanisms are not well understood, but is governed by a variety of forces including gravity, magnetic fields, rotation, thermal pressure, and turbulence. In addition, discrete sources inject energy into the clouds in the form of winds producing systematic motions and shocks. A highly "clumpy" structure may reflect gravitational fragmentation or the presence of turbulence resulting from the cascade and redistribution of energy injected on different scales. In contrast a highly filamentary structure might result from magnetic fields. Observers and theorists have sought the means to infer the operating forces and dynamical processes from an analysis of cloud structure. Recently we suggested that Laplacian Pyramid Transforms, a form of nonorthogonal wavelet with multiscale properties, could be used to measure the structural and hierarchical characteristics of astronomical maps (Langer, Wilson, and Anderson 1993). In that paper we analyzed CO maps of B5, a small molecular cloud covering about one square degree of the sky. Here we apply these transforms to IRAS 100 μm infrared maps covering about 300 square degrees of sky and encompassing diffuse cirrus clouds and denser molecular clouds. We also discuss the types of multiscale measures that can be applied to astronomical maps to characterize their structure and properties.

Several approaches have been applied to measure map properties and to extract and characterize structural features from astronomical images of interstellar clouds. These structural analyses include a search for connected objects using intensity contours (Bazell and Désert 1988; Dickman, Horvath, and Margulis 1990; and, Williams, de Geus, and Blitz 1994), structure tree analysis (Houlahan and Scalo 1990 and 1992), Gaussian decompositions (Stutzki and Gusten 1990), and multiscale transforms (Langer, Wilson, and Anderson 1993). Mathematical measures of global map properties have also been used, including Fourier power spectrum (Green 1993), auto-correlation functions (Kleiner and Dickman 1987), wavelet transforms (Gill and Henriksen

1990; Abergel et al. 1995), and metric-space (topological) classification (Adams 1992, Adams and Wiseman 1994, and Wiseman and Adams 1994).

The best known example of the multiscale transform is the wavelet transform (Grossman and Morlet 1987; see also the reviews by Daubechies 1992 and Farge 1992). However, another form, the Laplacian Pyramid Transform may be better suited to analyze maps or images (Langer et al. 1993). Multiscale transforms provide a mathematically consistent way to measure map properties and extract structural fluctuations from astronomical images. The multiscale transform has been characterized as a generalization of the Fourier Transform, but one which, unlike the Fourier Transform, is capable of representing a function in terms of spatial and frequency localization. A key point to keep in mind is that the multiscale transforms respond to changes in the intensity of a function, that is they measure the regions which change strongly on a particular scale. *Because wavelets and pyramids preserve scaling, localized fluctuations of structures at different scales may be easier to identify in the transformed space than in the original (x,y) space.* Thus the wavelet and pyramid transforms are well suited to provide detailed information and deep insight into structure. Wavelets have been used to analyze complex astronomical data, including: galaxy counts (Slezak, Bijaoui, and Mars 1990; Martinez, Paredes, and Saar 1993); stellar photometry in globular clusters (Auriere and Coupinot 1989); ^{13}CO spectral data of the L1551 outflow (Gill and Henriksen 1990); photometric analysis of galaxies (Coupinot et al. 1992); cosmic velocity fields using galaxies (Rauzy, Lachièze-Rey, and Henriksen 1993); fluctuations in 60 and 100 μm emission of high galactic latitude clouds (Abergel et al. 1995); and, clustering of QSOS (Pando and Fang, 1995). The Laplacian Pyramid Transform has been used to analyze CO images of the molecular cloud B5 (Langer et al. 1993).

Here we apply a multiscale transform analysis of infrared emission from clouds in the North Polar and Chameleon regions using the IRAS Sky Flux plates and analyze their morphology, fractal structure, and global energy spectrum. One advantage of the IRAS maps over existing CO maps of the interstellar medium is that they cover a large region of the sky and span scales from a few arcminutes to tens of degrees. Furthermore, IR emission arises from all regions of both atomic and molecular gas, while CO only traces the H_2 regions. Another advantage is that the 60 and 100 μm emissions are mainly optically thin in these maps. Their disadvantages are the lack of velocity resolution which makes it impossible to separate different spatial components along the line-of-sight, and the uncertainties in converting 60 and 100 μm intensities to dust, and afterward, gas column densities.

Infrared 60 and 100pm IRAS maps have been analyzed for scale-dependent morphology by a number of authors using various algorithms to characterize the features. All these algorithms rely on connecting contours in the original (x, y) intensity maps (see also Williams and Blitz 1993; Williams et al. 1994). Bazell and Désert (1988) analyzed the fractal structure of interstellar cirrus using the Sky Flux plates for three regions, one above and one below the plane (b = +23° and -14°), and a third region at b= -400 containing two high-latitude MBM clouds. Dickman, Horvath, and Margulis (1990) analyzed IRAS images of five molecular cloud complexes (including the well known regions of Chameleon, p Oph, and Taurus), Both found a fractal structure for the clouds and concluded that the clouds were highly turbulent. However, they each found different scaling behavior, which is not surprising considering that one focused on molecular clouds and the other diffuse clouds. Chappell and Scalo (1993) have analyzed IRAS emission maps for the fractal structure in several cloud complexes. They found that all the regions have multi-fractal scaling, indicating that there is not a universal scaling law for these clouds. Our multiscale analysis of cirrus emission reveals a more complex structure than any of these analyses, but is consistent with the conclusions of Chappell and Scale. Our analysis goes further than any of these works in measuring the energy density (what Fargc calls the "excitation level") and global energy (power) spectrum of the maps. In addition we define an algorithm for extracting fluctuations and features in the clouds, and catalog their properties. This algorithm forms the basis for a set of statistical map measures which can be used to characterize astronomical maps.

First we review the Laplacian Pyramid Transform and develop at greater length the ideas presented in our earlier *Letter*. Then we present the 100 μm images of two regions for analysis and their corresponding amplitude maps in the multiscale transform domain. This presentation is followed by a discussion of the global space-scale energy spectrum and an analysis of the structures in the maps with regard to the distribution of local energy density, and intermittence, and the fractal properties as determined from the Hausdorff dimension.

2. MULTISCALE TRANSFORMS

The multiscale transform is important because the physical laws in many situations arc translationally invariant and have the same structure over many levels o! scale. This scaling is the source of the fractal $1/f$ structure observed in many situations in nature. in the physical domain, for example, wavelets provide a useful description of turbulence which contains localized features and hierarchical spatial scaling. The wavelet transform retains information about the spatial structure of the flow and the transform coefficients at a particular scale will bc large for features which vary strongly on that scale (Farge 1992). The structure of many astrophysical objects fits into this category. In most cases the features in an astronomical map that vary on a particular scale can be detected more readily by searching for variations in the wavelet coefficients at that scale because the wavelet transform uses functions that span all scales.

Multiscale transforms provide a means to decompose images into their spatial frequency components such that all spatial scales are treated in an equivalent manner. The concepts are equally applicable to data of any dimension, where each axis represents some continuous physical parameter such as spectra] wavelength, time, or in the case of images vertical and horizontal lengths or angular displacements. An intuitive grasp of the idea can be obtained in one dimension by considering the illustration in Figure 1. The horizontal axis represents a parameter such as space and the vertical axis spatial frequency. If wc consider a signal S(x) that has been bandpass limited by a fixed amount, then it can be represented by a uniform sequence of samples $S(x_i)$, as set by the Nyquist sampling theorem, with no loss of information. Now consider passing the signal through a bank of filters F_n that are scaled copies of one another, such that $F_n(k) = F_0(2^n k)$, where the scaling by factors of 2 is chosen for convenience. The output of each filter treats the signal in a scale invariant fashion because of the scaling relationship between the filters. The outputs of each filter must be sampled at a rate that is proportional to the corresponding bandwidth, hence each band is sampled at a rate that differs from its neighbors by a factor of 2, as illustrated in Figure 1. This method of signal decomposition is the basis of all scale invariant multiresolution representations such as Pyramids and Wavelets. The signal processing community have labeled them as a special class of subband encoding schemes.

The generality of this form of signal analysis is best illustrated by noting that biological sensory systems also utilize it because this property is true of the images of natural objects, as well as auditory signals including music. The spatial--temporal decomposition of images by the human visual system is based on filters with a Q-factor of about an octave, while the auditory system uses bandwidths that are about a factor of 10 smaller. The scale invariant nature of many physical processes is what makes these representations important. The statistics of the signals and the forms of the structures produced by these filters provide measures of how underlying physical processes change with scale. The coefficients in these representations are much more statistically independent of one another than they are in the original data formats, which leads to a rich set of localized descriptors of images and better data compression for storage.

The number of such multiscale decompositions is large since there are many filter designs whose scaled filter banks will cover the frequency range of interest with sufficient density to prevent loss of information. This means there is a multitude of possible multiscale transforms unlike the Fourier transform. The choice of which to use is determined by factors such as efficiency of computation, signal-to-noise ratios, information storage and the type of data analysis one wishes to perform. In higher dimensional spaces the choices for the shape of the filter becomes increasingly more flexible and hence increases the number of possible transforms. The orthonormal wavelets, which have recently received a lot of recognition, are a particular subset of the multiscale transforms. These provide critically sampled representations with minimal storage, as well as having some nice mathematical properties, but the constraint of orthogonality leads to filter designs that are not necessarily the best for many applications. There are a number of overcomplete transforms, such as the Laplacian pyramid, based on circularly symmetric filters, oriented pyramids, which have "wave] et" like filters, and a recent new class with a property called "shiftability" (cf. Strang 1989, Simoncelli et al. 1992) which may be better for image analysis.

Laplacian Pyramid transforms preceded and spurred the recent interest by mathematicians in the more formalized orthogonal wavelets. In practice the orthogonal wavelets have proven useful primarily in image data compression, while the Laplacian Pyramid has remained more useful for carrying out a variety of image analysis tasks. Below we review the properties of continuous and discrete wavelets. For readers interested in more mathematically formal reviews of wavelets we recommend Daubechies (1 992), Farge (1992), and Wickerhauser (1994) while for less formal discussions see Martinez et al. (1993) and Press et al. (1993). Additional information on Pyramids *can* be found in Strang (1989), Simoncelli et al. (1992), and Andre-son and Rakshit (1994).

2.1 Continuous Wavelet Transform

A Fourier transform decomposes a function $f(x)$ into a linear set of trigonometric basis functions (sines and cosines) with amplitudes defined by their Fourier coefficients,

$$\hat{f}(k) = (2\pi)^{-1/2} \int_{-\infty}^{+\infty} f(x) e^{ikx} dx \qquad (1)$$

Unfortunately e^{ikx} oscillates forever and the information content of $f(x)$ is delocalized among all the spectral coefficients $\hat{f}(k)$. Furthermore, it is difficult to identify localized features in x space by searching through the k *space* because the Fourier Transform spreads power throughout all of k space. Such transform properties are not very useful for real astronomical images which contain a great deal of localized structure. One way to achieve localization is to use a window to isolate the portion of the frequency or spatial scale of interest (e.g. $w(x) = 1$, $0 < x < 1$, and zero elsewhere; or the Gabor window transform - see Martinez et al. 1993).

In contrast to the windowed transform multiscale transforms use a variable window size that covers all scales and localizes information in both space and scale. The basic continuous Wavelet transform has the form

$$\tilde{F}(s,x') = \int_R F(x)\,\psi_s(x,x')\,dx \tag{2}$$

where the analyzing functions $\psi_s(x,x')$ are generated by continuous translations and dilation of a "Parent" function

$$\psi_s(x,x') = s^{-1/2}\,\psi\left(\frac{x-x'}{s}\right). \tag{3}$$

The dilation factor s spans the range of scale-space, x' moves the center of the localized wavelet, and R is the interval over which the integral is taken. (Here we restrict the representation to one dimension.) The condition that the mean value of the "Parent" function over x must be zero, $\int_R \psi(x)dx = 0$, along with a localization constraint, makes these functions have a local oscillatory shape, hence the name Wavelets. The localization is related to the admissibility condition,

$$(2\pi)\int_R \left|\hat{\psi}(k)\right|^2 |k|^{-1}\,dk < \infty \tag{4}$$

where $\hat{\psi}(k)$ is the Fourier Transform of $\psi(x)$

$$\hat{\psi}(k) = (2\pi)^{-1}\int_R \psi(x)e^{-ikx}\,dx \tag{5}$$

The best known examples of a continuous wavelet transform in astronomy is the Marr, or "Mexican Hat", wavelet, which in one dimension has the form,

$$g(z) = (1 - z^2)e^{-z^2/2}, \tag{6}$$

where z = (x – b) /s and s and b are the dilation and translation terms, respectively (cf. figure 1 in Martinez et al. 1993).

Wavelets have the useful property that they preserve scaling behavior and are sensitive to signal variations but not constant behavior. If the function is smooth locally then the wavelet coefficient will not vary much, whereas it will change significantly for large or singular behavior in $f(x)$. The Fourier Transform is contained in the Wavelet transform and remains useful for harmonic analysis or when local information is not needed. Furthermore, the wavelet coefficients can also be defined in terms of the Wavelet transform of the Fourier coefficients,

$$\tilde{f}(l,x') = \int_R \hat{f}(k)\,\psi^*_{lx'}(k)dk\ , \tag{7}$$

analogous to filtering $\hat{f}(k)$ with a filterbank defined by $\psi^*_{lx'}(k)$. The original function can be reconstructed using an inverse transform,

$$F(x) = \int_0^{+\infty} \int_R \tilde{F}(s,x')\phi_s(x,x')dx'ds \tag{8}$$

The reconstruction imposes the following condition between the analysis functions $\psi_s(x, x')$ and the synthesis functions $\phi_s(x, x')$

$$\int_R \psi_s(x,x')\phi_{s'}(x',x'')dx' = \delta(s - s')\delta(x - x'') \tag{9}$$

For the class of orthonormal Wavelets $\phi_s(x, x') = \psi^*_s(x, x')$.

2.2 Discrete Wavelet Transform

The discrete Wavelet transform can be thought of as a set of samples of the continuous coefficients $\tilde{F}(s,x)$, taken at the scales $s = 2^l$ and points x = n, which we denote as $F_l(n)$. While the scaling between levels need not occur by a factor of 2, this scaling is generally always used because of the computational advantages it provides. The equations for computing the discrete coefficients and their inverse are

$$\tilde{F}_l(n) = \int_R F(x)\psi_l(x - n)dx \tag{10}$$

$$F(x) = \sum_{l,n} \tilde{F}_l(n)\phi_l(x - n), \tag{11}$$

where the translational invariance is made explicit by using $(x - n)$ in place of (x, n).

The reconstruction of $F(x)$ from the coefficients, or amplitudes, $\tilde{F}_l$ (n), can be as precise as one requires if the sampling rates satisfy the appropriate requirements, as described in detail by Daubechies (1992). An intuitive notion of this transform can be obtained by thinking of the analysis functions $\psi_l(x)$ as a bank of filters, which are all scaled copies of one another with a bandwidth of about an octave. The outputs of these filters are sampled at a rate that satisfies the Nyquist criterion, leading to a sampling rate that goes inversely with 1. The synthesis functions, $\phi_l(x)$, that provide the means to reconstruct the original function can be thought of as interpolating functions, where their form depends on the input filter analysis functions.

Usually the input function is provided as a set of samples (as in a discrete image) rather than as a continuous function. In order to apply the Wavelet transform one should use the information about how the samples were gathered to create the appropriate interpolating function to resynthesize the input. This information is seldom, if ever, used. instead one almost always implicitly assumes that $F(x) = \sum_i F_i \delta(x-i)$ and then applies Eq (10). This leads to a set of discrete filtering operations to compute the Wavelet amplitudes $\tilde{F}_l(n)$ of the form

$$\tilde{F}_l(n) = \sum_i \psi_l(i-n) F(i)$$

$$F(i) = \sum_{l,n} \phi_l(i-n) \tilde{F}_l(n) \qquad (12)$$

2.3 Fast Discrete Wavelet Transform

The direct computation of this discrete transform (Equation 2) is computationally expensive because the size of the filters becomes very large at low frequencies. The fast discrete Wavelet transform reduces the computation time by decimating the data at different stages of filtering. This approach is based on the observation that the first band, *1::0*, contains most of the information in the top octave in the frequency domain, while all the rest of the coefficients, $l > 0$, represent the information in the lower half. Thus by starting with the highest frequency one can extract this information at successive stages of analysis and work with progressively fewer samples. A recursive set of rules are used, which starts with a set of input samples, Go(i), and proceeds with the following operations

$$\tilde{F}_l(n) = \sum_i \psi(i - 2*n)\, G_l(i)$$

$$\tilde{G}_{l+1}(n) = \sum_i \omega(i - 2*n)\, G_l(i). \tag{13}$$

where ψ and ω are equivalent to high and low pass filters. The highpass filter ψ and low pass filter ω are carefully chosen to make sure the resulting ;;(n) create a representation of a discrete Wavelet transform. The factor of 2 on the right is used to indicate that the samples on the left are taken at half the density of those on the right (called decimation). This operation is repeated in increments $l + l + 1$, until there are only a few samples left in the last G_l, where edge effects will dominate the results. Because the number of samples in G_l is halved at each stage, the total computation required to carry out this procedure in one dimension scales as $1 + 1/2 + 1/4 + 1/8$ . ...= 2. This clearly results in handling each level of resolution in an equivalent fashion.

The fast discrete Wavelet transform has proven to be very useful in compressing data that has a $1/f$ spectral distribution, but there are problems in applying this technique for data analysis. First of all the subsampling causes appreciable aliasing, which is acceptable for data compression since it is encoded, and hence can be removed. There are, however, potential problems when the goal is to compare a localized measure of the variance across scale and space. Aliasing can cause the local squared amplitudes to change by 25 percent, or more, when the input image is moved by a single pixel. A second problem with the discrete orthonormal Wavelets is that no one has discovered how to create them in dimensions higher than 1 other than using product functions. Thus, in 2D the filters utilized in each stage of Eq (13) are of the form $\psi(x)\psi(y)$, $\psi(x)\omega(y)$, $\omega(x)\psi(y)$, and $\omega(x)\omega(y)$ where the last pair is used to create the cascading low pass versions G_l. This results in the transform being sensitive to orientation.

2.4 Laplacian Pyramid Transforms

As indicated above one of the major difficulties with the discrete orthogonal wavelets is that while their basis functions display shift and scale invariant properties, the coefficients in these expansions do not. in other words, the information in the wavelet subbands is unstable under translations of the input signal (cf. Strang, 1989; Simoncelli et al. 1992). This limitation may be problematical for signal and image analysis. In brief, these difficulties arise because the orthogonality requirement is also a constraint of critical sampling and this produces aliasing in discrete transforms. That the power within a given scale is not invariant to translations of the input which should be enough to make one wary in applying discrete wavelets. This problem also exists for the scale and orientation parameters in complex wavelet transforms, so that two-dimensional wavelets do not behave well under rotations and dilations of the input signal. Laplacian Pyramid Transforms overcome the problems associated with wavelet transform analysis of images by relaxing the critical sampling constraint, that is orthogonality, and by sampling signals at the Nyquist sampling rate. Simoncelli et al. (1992) have defined transforms that are stable under translations as "shiftable" (other operations have analogous properties of "steerability" and “orientability”). For pyramid transforms the coefficients in the expansion display shift and scale invariant properties.

The Laplacian transform, which preceded the orthogonal Wavelet transform in image analysis, largely solves the two major difficulties discussed above (Burt and Adelson 1983). The Laplacian transform is an overcomplete, non-orthogonal Wavelet transform, which are formally called frames by mathematicians. The structure of the transform is similar to that of Eq (13), and in two dimensions is given by

Something seems wrong here.

$$G_{l+1}[n,m] = H * G_l[2*n, 2*m] \qquad \text{Low Pass}$$

$$L_l[n,m] = G_l[n,m] - H * G_l[n,m] \qquad \text{Band Pass} \qquad (14)$$

where H is a smoothing filter, l labels the level of the filtering, G_0 is the original image, $H * G_l$ is used to denote a low pass convolution, and after each stage of filtering l is incremented $l \to l + 1$. (The notation F in Equation 13 comes from the reference to the "fast" wavelet coefficients and L in Equation 14 to the Laplacian coefficients). If the lowpass filter H is circularly symmetric, i.e. Gaussian-like in shape, then all orientations are handled in an equivalent fashion. Since the band pass components are created by simply subtracting out the low spatial frequencies at each stage, the filter looks very much like the Laplacian operator. The set of bandpass, or Laplacian, coefficients, $L_l[n, m]$ from $l = 0$ to any level N, plus the next lower lowpass filter, or Gaussian, G_{N+1}, can be used to reconstruct the original data set. Surprisingly this is true for any filter, H, one chooses, but for the purposes of analysis it is important to use filter designs that are not only circularly symmetric, but also do a good job of reducing aliasing.

The major difference between the Laplacian Pyramid transform and the fast discrete Wavelet transform is that in the former, the bandpass components are *not* subsampled, while the lowpass components *are* subsampled. Since these transforms are utilized on data sets with a $1 / f$ structure there is always a considerable amount of low frequency power entering into the bandpass components, L_l, that will become aliased during the subsampling. Conversely, there is little high frequency information to be contaminated by subsampling in the lowpass versions. The number of coefficients created by this procedure in d dimensions is equal to $1 + 1/2^d + 1/2^{2d} + 1/2^{3d} \ldots = 1/(1 - 2^{-d})$, which is 2 in 1D and 4/3 in 2D. The overhead in higher dimensions is even less.

2.5 Gaussian and Laplacian Coefficients

There is another way to view the Gaussian and Laplacian coefficients that makes them special. The process of low pass filtering is a local averaging process, hence the G_l represents local mean values of the original function averaged over a length scale $\approx \lambda_0 2^l$, where λ_0 is the size of the pixel in the original data. The Gaussian Pyramid consists of taking the original image, labeled G_0, and generating a series of lower resolution images, G_n, by recursively lowpass filtering and subsampling by factors of 2 along each dimension, commonly called decimation by the digital processing community,

$$G_{\{l+1\}} = \text{Decimate}\left(H*G_l\right),$$

where $H*$ denotes a lowpass filter operation, This pyramid is not a representation of the data set as are the other pyramid transforms, but it is a very powerful tool for efficiently computing the mean values of map data on multiple scales. It is also an essential tool used in coarse to fine search strategies. The process is extremely efficient for computing these averages over large length scales.

The Laplacian components on the other hand are computed by taking the difference between each value and the local mean resulting in a quantity which is the deviation from the local mean. Laplacian pyramids are created by subtracting successive stages of the. Gaussian pyramid. These Laplacian pyramids are non-orthogonal, overcomplete scale invariant representations. They can be viewed as providing a measure of how the signal deviates from the local mean on multiple scales. The version of the Laplacian Pyramid used here is called an FSD (Filter, Subtract, and Decimate) pyramid (cf. Van der Wal 1991; Anderson and Rakshit 1994) which was also described in Langer et al. (1993). In the FSD pyramid we start with the original image, designated as $G_0(x, y)$, and apply the following rules recursively to create a sequence of lowpass images (or Gaussian levels) G_l (x, y) and bandpass images (or Laplacian levels) L_l (x,)):

$$\hat{G}_{l+1} = H*G_l \quad \text{Lowpass Filter}\}$$

$$L_l = G_l - \dot{G}_{l+1} \quad \{\text{Subtract}\}$$

$$G_{l+1} = \{\text{Decimate}\}\ \hat{G}_{l+1} \tag{15}$$

The filter operation $H*G_l$ involves convolving the image G_l with a lowpass filter H. In this paper we will use a separable filter, $H(x, y) = h(x)h(y)$, and adopt a five tap filter for h(x) having the tap values 1/16, 1/4, 3/8, 1/4, 1/16, which produces an approximately circularly symmetric filter in the spatial frequency domain. The Laplacian components, L_l, are computed by subtracting the low pass version from the unblurred one at each scale, This operation is equivalent to filtering with a "Mexican hat" or difference of a "Gaussian-like" shaped kernal. The blurred version, G_l is then subsampled by throwing away every row and column. This declination is justified because the lowpass filter reduces the spatial frequency content such that little aliasing is introduced by this process. Typically the final level N is set by stopping the process when the smallest dimension of the array G_{l+1} (x, y), would be no smaller than eight. Thus the Gaussian and Laplacian Pyramids provide the local first order simple statistics of mean values and variances, respectively, at each point and scale in the data set.

As discussed above it is the scale invariant nature of many physical processes that makes these representations important. The statistics of the signals and the forms of the structures produced by these filters provide measures of how underlying physical processes change with scale. The coefficients in these representations are much more statistically independent of one another than they are in the original data formats, which leads to a rich set of localized descriptors of images. The number of multiscale decompositions is large since there are many filter designs whose scaled filter banks will cover the frequency range of interest with sufficient density to prevent loss of information. This property means there is a multitude of possible multiscale transforms unlike the single basis for the Fourier transform, The choice of which filter to use is determined by factors such as efficiency of computation, signal-to-noise ratios, information storage and the type of data analysis one desires to perform. When one goes into higher dimensional spaces the choices for the shape of the filter becomes increasingly more flexible and hence increases the number of possible transforms.

Reconstruction of the original image can be achieved with an inverse transform from the set of L_l and $\hat{G_{l+1}}$ amplitudes,

$$G_l\,[n, m] = L_l[n,m] + (\text{Expand}\}\ G_{l+1}[n,m]$$

$$G_l[n,m] = L_l[n,m] +- \{\text{Expand}\}\left(L_{l+1}[n,m] + G_{l+2}[n,m]\right)$$

$$G_l[n,m] \approx \sum_{i=l}^{N} \{\text{Expand}\}^{i} L_l[n,m] \tag{16}$$

where the {Expand } operator increases the number of rows and columns by a factor of 2, inserts zeros in these, multiplies the original values by four, and smoothes the results with a low pass filter. The original image is generally reconstructed with some loss of information because some of the high frequency information is removed by the {Expand} operator. Part of this information can be recovered from low pass filtering the Laplacian,

$$G_l \approx L_l + H{*}L_l + \{\text{Expand}\}\ G_{l+1} \tag{17}$$

The reconstructed G_0 is reproduced to better than five percent on a pixel-by-pixel basis over the entire image and typically is lower than 2 percent (cf. Anderson and Rakshit 1994 for an evaluation of the implementation of different transforms for reconstruction).

It is also worth noting that

$$\left\langle G_l \right\rangle \approx G_{l+1} \quad \text{local average mean, and}$$

$$\left\langle L_l^2 \right\rangle = \left\langle \left(G_l - G_{l+1}\right)^2 \right\rangle \quad \text{local averaged squared invariance,} \tag{18}$$

and the complete set over all l leads to measures of these statistics at all scales.

2.6 Multiscale Transforms and Map Measures

Generally it is easier to solve the equations characterizing a physical system by choosing an appropriate basis function that represents the underlying structure and symmetry. In the cases where filters are used to extract solutions, or information, the choice of filter (or transform) introduces its own response to the transform coefficients. In hydrodynamical systems the variety of flows and structures is very large and one does not know *apriori* what type of filter to choose. We are faced with a similar problem for analyzing interstellar clouds where the equations governing the evolution of the medium are those of a rotating gaseous fluid, partially ionized, containing magnetic fields, and gravity. If interstellar clouds have simple wave motions then it may be appropriate to use a Fourier Transform to describe the structure as it yields well defined wavenumbers. However for vortices, turbulence, chaotic fields or hierarchical gravitational fragmentation the Fourier Transform is not a good transform to characterize structure. In these cases multi scale transforms are useful for analyzing turbulence or hierarchical fragmentation because they retain information about localized spatial structure and scalings.

Wavelets are useful descriptors of structure because they are: 1) linear; 2) covariant under translation and dilation; 3) differentiable, and, 4) space-scale invariant, i.e. conserve locality. Furthermore there is no loss of information in the wavelet transform and they conserve energy globally, so that the total energy can be written in terms of the energy at different scales. In addition, they can measure the local regularity of a function and characterize its functional space, thus allowing one to characterize fractals and multifractals. Farge (1992) defines a number of useful functional relationships for describing fields with turbulence, or “turbulent” like properties, based on wavelets. These are particularly useful measures and here we give the corresponding formulations for the Laplacian Pyramid transforms.

2.6.1 Space-Scale Global Energy Spectrum

The space-scale energy density in 1-D is

$$\varepsilon_l(x) = F_l^2(x) \tag{19}$$

while the space-scale global energy is given by

$$E = \int |F(x)|^2 dx = \sum_{l,n} \sum_{k,m} \tilde{F}_l(n)\tilde{F}_k(m)\Gamma_{l,n,k,m} \tag{20}$$

where $\Gamma_{l,n,k,m} = \phi_l^*(x-n)\phi_k(x-m)dx$. For a complete and orthonormal Wavelet $\Gamma_{l,n,k,m} = \delta_{l,k}\delta_{n,m}$ thus

$$E = \sum_{l,n} \left|\tilde{F}_l(n)\right|^2 .$$

We now identify the space-scale global energy (or power) spectrum as the sum only over n

$$E_l = \sum_n |F_l(n)|^2$$

and note that $E = \sum_l E_l$, For the LPT non-orthogonal representation the overlap factors are small and so we use the approximation

$$E_l \approx \sum_n |L_l(n)|^2 \tag{21}.$$

Note that $\varepsilon_l(x) = L_l^2(x)$ = square of local variance. Thus these energy measures are really measures of the variance at different scales.

2.6.2 Intermittency

The departure of the energy at each scale from an even spatial distribution in the map is called the local intermittence, $\iota_l(x_i, y_j)$. Intermittence is defined by,

$$\mathrm{l},(\mathrm{x}) = \frac{\left|\tilde{F}_l(x)\right|^2}{\left\langle \left|\tilde{F}_l(x)\right|^2 \right\rangle} \tag{22}$$

$$l,(x) \approx \frac{\left|L_l(n)\right|^2}{\left\langle \left|L_l(n)\right|^2 \right\rangle} \tag{23}$$

for the wavelet and LPT cases, respectively, where $(\ldots.\, .\rangle_x$ is an average over al the map. If all locations have the same energy spectrum, as is the case for the Fourier energy spectrum, then $l_l(x_i, y_j) = 1$. On the other hand if $l_l(x_i, y_j) = \beta >>1$ then at space-scale 1 the position (x_i, y_j) contributes β times as much as the average to the Fourier energy spectrum.

2.6.3 Space-Scale Contrast

Another important measure is the space-scale contrast, which is a logarithmic derivative of the wavelet coefficients (Farge 1992). It is particularly useful for detecting very weak coherent structures or embedded coherent structures, where traditional threshold techniques do not work very well (such structures do not have well defined boundaries). The space-scale contrast is

$$\mathrm{c},(\mathrm{n}) = \frac{\left|\tilde{F}_l(n)\right|^2}{\left\langle \left|\mathrm{F},(\mathrm{n})\right|^l \right\rangle} \tag{24}$$

$$C_l(n) \approx \frac{\left|L_l(n)\right|^2}{\left\langle \left|G_l(n)\right|^2 \right\rangle} \tag{25}$$

for the wavelet and LPT cases, respectively, and where $\bar{F}_l\,(\mathrm{x}) \approx \int_0^l \tilde{F}(l', x)\,dl'$ are the amplitudes for the Gaussian level G_l at scale 1. This measure is the ratio of the local squared variance over the local mean value.

Finally, it is possible to calculate the local scaling and singularity spectrum with an appropriate choice of multiscale transform (Farge 1992). These can be used to characterize the fractal and multi-fractal properties of a function. Here we do not calculate these properties directly, but instead analyze the local scaling using the Hausdorff dimension of the fluctuations.

3. RESULTS

To study the properties of infrared dust emission from clouds we have chosen IRAS maps of the Chameleon and the North Polar regions (centered at RA(1950) = 12^h and DEC(1950) = -80^o and RA(1950) = 0^h and DEC(1950) = 90^o, respectively) where line-of-sight confusion is minimized. A reasonable first approach is to restrict the multi scale analysis to the 100 μm maps and thus reduce the dependence of the results on specific dust models. We used IRAS Sky Flux maps each measuring 12.5^o on a side with 500 x 500 pixels. Although the pixel size in these maps is 1.5 arcmin the actual angular resolution is probably closer to the 3 or 4 arcmin resolution of the IRAS instrument at 100 pm. Figure 2 is a contour plot of the 100 μm images and shows the highly complex filamentary and globular nature of the emission plus small nearly "point-like" extragalactic sources. These maps show a great deal of structure on all scales and the variation in emission is either due to increased column density, changing dust grain distribution, or the presence of heating sources.

To produce the results in this paper we have used a package of programs that we developed under NASA's Astrophysics Data Program (ADP) called Astrophysics Pyramid Imaging Processing, or APIP. This package currently resides at IPAC and will be available to the general astronomical community in the near future. APIP contains many more multiscale transforms, image analysis tools, and map descriptors then used in this paper. We intend to describe these in a future publication.

[illegible]

3.1 Multiscale Transform Images

The multi scale LPT analysis of the 100 μm images generates an amplitude map at each space-scale (one for each of the basis functions). These are designated L_l with $l = 0$ to 5 covering the space-scales, $\lambda_l = 2^l \lambda_0$, corresponding to 1.5' to 48'. In addition there is one Gaussian map remaining after filtering, G_6 (the original image is labeled Go). As discussed above the Cl are mean values computed over regions that decrease in resolution by factors of 2 and the L_l provide the local deviations (fluctuations) from these multiscale values. The L_l images represent the detailed information in the original map and have equal positive and negative areas ($\sum_{i,j} L_l(x_i, y_j)$ = O). The final Gaussian map, G_6, which has a resolution of 96', is smooth and positive definite over the map. Figures 3a and 3b shows some of the Laplacian amplitude maps and the original IRAS map, Go, in the form of gray scale images. It can be seen that the most prominent features in the original IRAS 100 μm maps stand out clearly in the different scale-space maps, separated at different scales. More important, however, is that many features which are not readily evident in the original maps are prominent here, especially small structures (including several galaxies and some residual striping evident in the $1 = O$ and 1 maps). For comparison Figure 3c shows a discrete wavelet transform of the Chameleon region for $l = 1$ using the Daubechies wavelet four calculated in two dimensions (see Daubechies 1992 and Press et al. 1993). Note that the Daubechies wavelet amplitude image has a weaker correspondence between the original image and the transform amplitudes. This difference illustrates the care that must be taken in the choice of "filtering" to analyze maps.

3.2 Global Space-Scale Energy Spectrum

The space-scale energy density $\varepsilon_l(x_i, y_j)$ is the starting point for several important measures of the map properties discussed above. We generate ε_l (x_i, y_j) by squaring the amplitude for each pixel of the $L_l(x_i, y_j)$ map and some examples are shown in Figure 4 in color several (these are in their decimated form and are smoothed for display purposes). The simplest measure is the global energy spectrum which helps to classify the map properties by giving the power distribution of the entire map at different scales.

We have calculated the global space-scale energy spectrum E_l for the entire 12.5° x 12.5') area of the maps of Chameleon and North Polar regions. These are plotted in Figure 5 along with E_l for a random image and for a ^{13}CO integrated intensity map of the Perseus region (Langer et al.

1995). The random plot allows us to compare the 100 μm emission to that of an image with no large scale structure. (For purposes of comparison the energy spectra have been normalized to 1 by dividing by the values at E_0.) It can be seen that for the random image E_l falls off very sharply with 1, $E_l \propto l^{-3}$ over the range 1 = O → 3. In contrast the infrared and ^{13}CO emission maps, which trace coherent structures of the cloud, increase by an order of magnitude from l = O → S. Typically at the smaller scales, l = O → 1, one has to consider the effects of noise in the maps on the power spectrum. The noise contribution will depend on the overall signal-to-noise in the maps and the extent of noisy or emission free regions. For these IRAS maps it is not significant on global scales (summed over the entire map) but can be important locally depending on map position (cf. Abergel et al. 1995).

Closer inspection (Figure 5 lower panel) shows significant differences among the global space-scale energy spectra for these regions. The North Polar region, which is the most diffuse of the three regions, has the steepest spectrum and thus relatively less of the power is in small features. The Chameleon region has more gas in higher density material and this characteristic is reflected in the flatter spectrum. Finally, ^{13}CO traces much higher density material on average than 100 μm emission, is more compact, and is generally restricted to the dense interiors. This selectivity is apparent in the Perseus spectrum which is very flat at small scales (l = O → 1) and peaks at 1 =4. It shows the tendency for clumping to take place at small scales and for most of the power, and hence most of the material, to be in features with space-scale size ≈ 16 arcmin.

3.3 Statistical Map Properties

There is a wealth of information for each of the maps, much more than can reasonably be presented here. Obviously there are so many fluctuations/features, especially at small scale, that it is impossible to study each one in detail. Instead we have opted for a statistical approach for understanding the properties of each map, To catagorize and compare maps we need to develop local measures of the images. The starting point for this approach is the space-scale energy density

$\varepsilon_l(x_i, y_j)$ shown in Figure 4. To develop a descriptor of the maps we first need to identify and categorize all the distinct features in these maps (one for each space-scale. l).

Astronomers have generally relied on techniques to find features in astronomical images, such as thresholds and other filtering methods, that apply to sharp contours. However, molecular cloud structures, fluid flow, turbulence, etc. have coherent structures that do not have sharp boundaries. In these cases multiscale transforms provide a better approach because of their filtering and scaling properties. Techniques that extract interstellar cloud features using contours generated by cutting the original intensity maps at constant amplitude have drawbacks. The contours are generally poorly defined because clouds most likely have features embedded on a range of scales, In Section 2 we discussed how multi-scale transforms are sensitive to variations in the function but respond only weakly to slow global variations at their particular scales. In the infrared maps the features at each scale are embedded one within the other, and/or superimposed along the line-of-sight. The Laplacian amplitude maps measure the localization of features on different scales at each position. Therefore these features should be separated by their space-scale transforms into the different Laplacian amplitude maps, L_l, and energy density maps, ε_l.

The amplitude of the transform coefficients measures the variations in the function at a particular scale and position. Thus the transition from negative to positive amplitudes, that is the zero boundaries in the transform map (Laplacian amplitudes) at each scale (i.e. each Laplacian map), should define the regions of localized features in, $L_l(x_i, y_j)$. Note that a closed zero boundary in the Laplacian amplitude map is also a zero boundary in the space-scale energy density map ε_l. Thus identifying the closed zero boundaries in the Laplacian or energy density maps provides a well defined algorithm for isolating separate space-scale fluctuations.

We can identify the different map features by finding all the zero boundaries in L_l (xi, y_j) or El (x_i, y_j). The zero boundaries in $L_l(x_i, y_j)$ can easily be found from the crossings from positive to negative amplitudes, which is computationally simple for discrete images. However, in practice the corresponding zero boundaries in El (xi, y_j) do not exist because of the discrete nature of the amplitude of the pixels (i.e. very few pixels actually have a value of zero). Instead we can either find the zero crossings in $L_l(x_i, y_j)$ and project them onto the $\varepsilon_l(x_i, y_j)$ map or find an approximate solution by cutting the $\varepsilon_l(x_i, y_j)$ map with a constant plane having a small positive value. This threshold will isolate the features in $\varepsilon_l(x_i, y_j)$ space. (For each space-scale image we use the discrete pixel images and not those in Figures 3 and 4 which have been smoothed for display purposes). The derived map features can be cataloged in terms of their properties at each scale l: number, N_l, perimeter, P_i, area, A_i, where i labels all the isolated features in the maps. The local energy spectrum, $E_{l,i}$, is given by

$$E_{l,i} = \oiint_{\Omega_i} \left|\phi_l(x, y)\right|^2 dxdy \tag{26}$$

where $\phi_l(x, y)$ = amplitude of the Laplacian basis function for space-scale l at (x, y). The integration is taken over the zero boundary Ω_i of each feature labeled with the subscript i where the sum is over all pixels n contained within the boundary Ω_i. Note that the local energy spectrum is not the same as the global energy spectrum or local energy density. Instead it is the portion of the global energy at space-scale λ_l of a feature within boundary Ω_i.

In addition we have found the following two quantities, integrated intensity and average intensity useful for identifying noise features and extragalactic objects.

intensity:
$$I_{l,i} = \oiint_{\Omega_i} \phi_l(x, y)dxdy \tag{27}$$

Average Intensity:
$$\left\langle I_{l,i} \right\rangle = A_i^{-1} \oiint_{\Omega_i} \phi_l(x, y)dxdy\,. \tag{28}$$

3.3.1 Number of Features

There are two practical problems with identifying a fluctuation or feature in the maps, one associated with noise and the other with the pixel size. Noise in the original maps will result in regions of positive and negative amplitude in the Laplacian images covering small areas, especially at the smallest scales. These will be extracted as a feature by our zero crossing algorithm. Furthermore, while the pixel size in our maps is 1.5 arcmin the resolution of the IRAS Sky Flux images at 100 μm is roughly 3 to 4 arcmin so that some features with small areas may not be real. We can eliminate almost all of the noise clumps by considering only closed features with area, $A \geq 15$ arcmin^2 corresponding to the IRAS 100 μm beam (see also the method discussed by Abergel et al. 1995). This approach significantly reduces the number of small noise features that are extracted by our feature finding algorithm. In other maps where the pixel size equals the resolution we can still set a lower limit on area. However, as the correct choice cannot be exactly known, some real but small features will be excluded. Map regions with poor signal-to-noise have the worst problems in this regard.

The number of distinct features in the energy density maps are plotted in Figure 6 for two cases: (1) all fluctuations (pixel area >2,25 arcmin^2), and, (2) only for features greater than the IRAS resolution (area > 15 arcmin^2). At large space-scales ($l \geq 2$) the two regions have a very similar number of features, whereas at the smallest space- scale the North Pole region has roughly twice as many features as the Chameleon region. The majority of features in the 1 = O maps (> 80 percent) have very small areas (≤ 15 arcmin^2) less than the resolution of the IRAS Sky Survey maps and are probably noise. If even a modest fraction of them are real then the majority of the smaller features in the space-scale maps are weakly emitting, low density fragments.

The average intensity, (1), can also be used to eliminate features produced by noise in the original images. In the JR cirrus maps $\langle I \rangle$ tends to fall within a fairly well defined range for most features with good signal-to-noise, while noisy regions with poorly defined features have small values of $\langle I \rangle$. We tested this assumption by inspecting $\langle I \rangle$ in regions with very little dust emission (poor signal-to-noise) and then chose an average value of $\langle I \rangle$ as a threshold to decide whether a feature anywhere else in the map is real or not, In the IRAS maps where the signal-to-noise is generally very high almost all these low amplitude features are eliminated from consideration just by our constraint on the minimum area (> 15 arcmin^2). We have also found $\langle I \rangle$

to be useful for identifying features that may not be cirrus clouds, for example galaxies in the IR maps stand out as having much larger $\langle I \rangle$ than average at small scales.

Figure 7 shows the relationship of $\langle I \rangle$ with area for Chameleon and North Pole regions only for positive amplitude features and for $A_i > 15$ arcmin^2. Note that $\langle I \rangle$ stays in a fairly narrow range and tends to increase with area. Several features appear clearly in both regions for small areas, having about an order of magnitude larger value than average. Most of these positive amplitude features can be identified with galaxies, they have sharply peaked emission over a small size. Another set of points have very small $\langle I \rangle$ at small to modest area, especially in the North Pole maps, These are either remaining noise features or arc regions with low column density, and perhaps represent diffuse gas. They only make up a few per-cent of the features.

Another problem inherent in the analysis of the properties of the fluctuations is the discrete nature of the pixels. In calculating the perimeter and area we follow the boundaries of the pixels (squares in this case), whereas the real cloud features are continuous boundaries. In this case the perimeters and areas will be overestimated, with the former suffering more severely. For example, a diagonal line will be covered by a diagonal of pixels and tracing the edges of these defining pixels overestimates the length by $\sqrt{2}$ (an average over all angles of inclination produces an average overestimate of $4/\pi$). The overestimate of the area will be small for regions covered by many pixels, but can be roughly a factor of two for regions covered by only a few pixels. In this paper we have not attempted to correct for the discrete nature of the boundaries.

3.3.2 Distribution of Local Energy

The local energy of all the fluctuations versus area is plotted in Figure 8 for all of the space-scale maps combined and shows that local energy grows rapidly with area, $E \propto A^{1.5}$. The larger features have more local energy not only because they are larger but because the larger features are intrinsically more intense. The smaller features contain less emission, less concentration of material and/or are colder. A plot of their number distribution shows the peak in the local energy distribution for the North Pole region is much less than that for Chameleon (Figure 9). Both regions have features with very large, but similar, values of local energy. The North Pole region is cut off more sharply at small values mainly because of the truncation of small area features which arc more prominent in this region.

3.3.3 Hausdorff Dimension

One measure of the scale dependent morphology, or fractal structure, of the cirrus clouds is the Hausdorff dimension, D, (cf. Bazell and Désert 1988, Dickman et al. 1990). Ideally, the geometrical structure and the scale dependence provides information about the forces at work in the cloud. D is defined from the area-perimeter relationship $A^{1/2} = KP^{1/D}$, to be

$$D = 2\frac{\partial \log P}{\partial \log A} \tag{29}$$

Most authors use a linear fit to a plot of log(perimeter) versus log(area) where the slope yields $D / 2$ and the intercept equals $-D(\log K)$. Regular geometrical objects (circles, ellipses, squares, etc.) all have $D = 1$ (i.e. the same scaling) but different intercepts (i.e. K depends on shape). The scaling relationship expected for Kolmogorov turbulence (incompressible, homogeneous, isotropic turbulence) is $D \approx 4 / 3$ (see the discussion by Dickman et al.). Filamentary structures that scale only with length, on the other hand, have $D \approx 2$, as would be characteristic of gas supported by ordered magnetic fields. We have evaluated the perimeter-area relationship for the energy density maps using the features derived for the localized energy. In Figure 10 we show plots of log P – log A for the space-scales $1 = 1$ and 2 for both maps. D derived from a linear fit to all of the log P – log A graphs is plotted in Figure 11 as a function of space-scale 1 and the corresponding fits are shown in Figure 10. The value of D is large at small space-scales and decreases at the largest scale.

It is readily apparent, however, that a linear fit does a poor job of matching the log P – log A plots at small space-scales in Figure 10. Closer examination shows log P – *log A is nonlinear* and thus there is no single scaling relationship, rather the IRAS emission is multifractal for both map regions. We find that a polynomial is required to fit the data for small space-scales and these are shown for $l = 1$ and 2 in Figure 10. At larger scales (for $l = 5$ and, sometimes $l = 4$) only a linear fit can be made because there are not enough features in the larger scale maps to make an accurate polynomial fit. Most of the variation in D is due to changes in the scaling relationships and the structural nature of the objects embedded in the images, but some is due to the properties of the filters and the use of discrete pixels. For the very smallest areas the only possible perimeter-area relationship is that for regular geometrical objects because one to three pixels can only combine to make squares, rectangles, etc. all of which scale with dimension $D = 1$. Furthermore, the very largest areas possible at small space-scales will be filamentary or web-like because we use separable filters $H(x, y) = h(x)h(y)$. As discussed above filaments are extracted with $H(x, y)$ wherever a region varies significantly in only one dimension. The scaling for filaments yields a value of D approaching 2.

The relationship of D versus A derived from a polynomial fit for equation (29) is shown in Figure 12 for a few maps. The smallest objects remain somewhat regular, the largest filamentary, and those in between have a fractal-like geometry. We calculated the number of features in each energy density map as a function of the fractal dimension D. As shown in Figure 13 $N(D)$ decreases with D and most of the features in the maps (excluding 1 = O) have either regular structures, $D \approx 1$, or turbulent structures, $D \approx 1.2 - 1.4$. Only few features have the characteristics of filamentary structures with a nearly linear scaling.

3.3.4 Intermittency

To measure the degree of localization of energy in the IRAS maps we evaluated the intermittence and characterized it locally over regions similar to those defined in the energy density maps,

$$\langle \iota_{l,i} \rangle = \oiint_{\Omega_i} \iota(x, y)\,dx\,dy \qquad (30)$$

We isolated all connected regions above a constant plane defined by $\langle \iota_l(x_i, y_j) \rangle \geq 0.25$ for small space scales and $\langle \iota_l(x_i, y_j) \rangle \geq 2.0$ at 1 = 4 and 5. The different threshold values are required because the large space-scale maps merge into very few features at low threshold due to the discrete nature of the pixels. Several of these distributions are shown in Figure 14. In the Chameleon maps it can be seen that for $\langle \iota_{l,i} \rangle$ most fluctuations have small values of less than one over a large range of area, while a few features have very large values. The smaller fluctuations tend to cluster around a constant value with $\langle \iota_l \rangle$ less than one. Some features, most likely extragalactic, have very large values of $\langle \iota_l \rangle$ at small areas. For the larger space-scales the distributions tend not to have much correlation. There is a slight trend in most of the maps to have the average intermittency increase at large areas. However, these features may not be distinct objects as many of them are due to overlapping emission from clouds along the line-of-sight.

3.3.5 Area and Intensity Distributions

To gain further insight to the properties of the Laplacian amplitude maps we have evaluated the distributions in A, I, and E for each space-scale. Differences between the Chameleon and North Pole regions are illustrated in Figure 15 for two scales, l = 1 and 4, corresponding to the small and large scale structures. For l = 1 the distributions for area, intensity, local energy for the regions are similar in shape, but the North Pole tends to have (on average) smaller features, lower intensity and local energy, yet many more features at small scale. The distribution in area shows that the number of features decreases significantly with increasing area and that only a few features are very large. It might seem surprising at first that a space-scale of only 3 arcmin would produce a few features with areas of order 10^4 arcmin^2, however the multiscale filters (here the separable filters $H(x,y) = h(x)h(y)$) will produce a response as long as the intensity varies along one dimension. (We intend to report on the use of orientable filters which should not produce such features, in a future publication.) Thus long filamentary- or thread-like structures will be extracted with large areas but small scales in only one direction The Chameleon and North Pole maps tend to exhibit the same behavior at large space-scales, as indicated by the 1 = 4 distributions, that is they are broad and flat, and hence show no preference for features of a particular size. These large area features are probably independent of one another in a dynamical sense, however, it should also be borne in mind that the number of features is statistically small at these large scales.

3.4 Features Reflected in Positive and Negative Amplitudes

Is there any physical difference in the closed features defined by the areas of positive and negative amplitudes? By definition the mean value of the wavelet and pyramid coefficients over the entire sample domain is zero so that the sum over the positive and negative amplitudes are equal,

$$\sum_{\phi \geq 0} \phi_i = \sum_{\phi \leq 0} \phi_i \, . \qquad (31)$$

However, the corresponding space scale energy densities (or variance) are not in general equal, that is

$$\sum_{\phi \geq 0} |\phi_i|^2 \neq \sum_{\phi \leq 0} |\phi_i|^2 \qquad 32)$$

This difference is most clearly illustrated for the extragalactic features in the IRAS maps, which are small intense localized regions of emission and nearly pointlike at the IRAS resolution. In the l = o amplitude map, $L_l(x_i, y_j)$, the extragalactic features appear with a large positive amplitude over a small circular area surrounded by a larger area ring of small negative amplitude. In the l = O energy density map, ε_l(xi, y_j), galaxies appear as an intense positive circular feature surrounded by a weaker intensity ring.

In Figure 16 we plot the ratio of the power contained in features with positive amplitude to the total power in the map at each space-scale. In both maps, on a global basis, $\sum_{\phi \geq 0} |\phi_i|^2 > \sum_{\phi \leq 0} |\phi_i|^2$. In Chameleon, which has more localized emission region, this fraction dominates at all space-scales, especially for $l \leq 4$, while in the more diffuse North Polar region it is less dominant on a global basis. Visual inspection of the energy density maps in Figure 4 with the original contour maps (Figure 2) shows a strong relationship between their structures.

Features at each scale have more sharply defined peaks in the energy density space-scale maps than the Laplacian maps or even the original data. Therefore, to first order the positive features in the amplitude map can be identified with the localized physical objects.

3.8 Mass Spectrum

Visual inspection of the Laplacian amplitude images for the IRAS maps, as well as the earlier study of CO emission maps for the cloud 135 (Langer et al. 1993), shows a correlation between regions of enhanced cloud material and positive amplitudes in L_l, and bubbles or valleys in emission and negative amplitudes in L_l. Because the Laplacian Pyramid Transform removes the amplitudes at each scale before operating on the next scale it acts as a decomposition of the original map. Therefore, to first order we can use the intensities in the positive amplitude maps to estimate the mass distribution of the dominant features in the maps. The mass spectrum of the clumps, or fluctuations, is an important cloud property, which reflects the fragmentation, coagulation, and turbulence of the gas. For the IRAS 100 μm maps we assume the mass is roughly proportional to the dust emission assuming a constant heating rate. The mass spectrum can be approximated by the distribution of intensity, 1, of features derived from the Laplacian maps (cf. Figure 9). In Figure 17 we plot the number of features as a function of intensity I. Both regions show a similar distribution, with a peak at modest, but different, values of I. Fits to the $\log N - \log I$ plots at small and large values of I give roughly similar results: for the high end of the mass spectrum, $N(I) \propto I^{-0.55}$ and $N(I) \propto I^{-0.58}$ for the Chameleon and North Pole maps, respectively; the corresponding fits for the low end are, $N(I) \propto I^{1.8}$ and $N(I) \propto I^{1.65}$. The similarity in the slope for large intensity implies a common fragmentation mechanism and source of the fluctuations in both regions, The break in the slope, which occurs at a slightly different I in both regions, is significant in that the lowest intensity fluctuations perhaps do not form by hierarchical fragmentation but arise from some other formation mechanism, for example turbulent fluctuations in the gas clouds leading to transient features. This picture would be consistent with our results for the Hausdorff dimension since most of the lowest intensity features in the $l = 0$ map have a value $D \approx 1.2 - 1.4$.

The mass distribution of clumps in clouds has also been derived using molecular line tracers (mainly CO, but some CS) by Stutzki and Güsten (1990) and Williams, de Geus, and Blitz (1994). The former have analyzed their maps using a sum of tri-axial gaussians (their routine is called Gaussclumps) while the latter have developed a program called Clumpfind which is based on searching for contours which divide the peaks and valleys in the data cube. Williams et al. find $N(M) \propto M^{-0.32}$ for the Rosette molecular cloud and $N(M) \propto M^{-0.44}$ for the Maddelana molecular cloud. Stutzki and Güsten found $N(M) \propto M^{-0.72}$ for M 17 using Gaussclumps while Langer et al. found a similar relationship for B5, $N(M) \propto \mathrm{M}^{-o''so,}$ using the multi-scale approach discussed here. If we assume that these differences arc real, anti not an artifact of the various algorithms used to extract the mass spectrum, then there is a difference in the formation process for clumps and fluctuations among the different types of clouds.

The number of features as a function of local energy is plotted in Figure 18. Both distributions have nearly the same slope, $N(E) \propto E^{-0.59}$ and $N(E) \propto E^{-0.54}$ for Chameleon and North Pole. Thus in a statistical sense each region is divided up into features with similar relative "power", though the Chameleon region has larger range of local energy.

4. SUMMARY

Multiscale transforms represent map information in a form that lends itself to disentangling the underlying fluctuations in the structure. In this paper we have extended the usc of Laplacian Pyramid Transforms presented in an earlier work (Langer, Wilson, and Anderson 1993) to large scale IRAS 100 μm maps of infrared emission of the Chameleon and North Polar regions. The LPT technique consists of a multiscale filtering *and* decomposition of the intensity maps which represents detailed information on each scale by a function, called the Laplacian of the image, L_l at a scale l, and the smoothed information at that scale by another function, the Gaussian, G_1. The set of Laplacian maps at different logarithmic scales and the residual Gaussian after filtering out all the detailed information successively constitute the space-scale representation of the map. These representations and the corresponding energy density maps provide a rich set of descriptors with which to characterize the map properties. We have drawn on analogous properties of wavelet transforms and their application to turbulence to define a set of map measures: space-scale energy density, global energy spectrum, local energy spectrum, and intermittency. In addition we have used the zero crossings in the amplitude and energy density maps to define the physical boundaries of map fluctuations and features. For each of these we evaluated their area, perimeter, and local space-scale energy. The distribution of these quantities provide a statistical measure of the maps, which may lead to a better understanding of the physics and dynamics in the interstellar medium and in interstellar clouds.

The Chameleon and North Pole regions have different global energy ("power") spectra, and this difference is a measure of the degree to which condensation has taken place. Chameleon has relatively more energy density at small space scales (small features) than the North Pole, but not as much as the molecular material in the Perseus region. The distributions in average intensity and average intermittency per feature in the two maps supports this point of view and indicates that Chameleon has fewer low contrast features, and more higher density fragments. This result is suggested by the much larger spread in the average intermit tency (11) in the small space-scale maps of the North Pole region. The differences in the global space-scale energy spectrum and intermittency maps suggests that the clouds in these two regions either have different forces dominating their structure and/or are at different stages of evolution.

Our results for the Hausdorff dimension in the IRAS data ~~is~~ are quite different from -that //as of X previous authors. In our multi-scale analysis the average Hausdorff dimension D as determined from a linear fit to log P – log A *(see* Figures 10 and 11) ranges from 1.3 to 1.7 for Chameleon and 1.2 to 1.7 for the North Pole cirrus features, with typical values about 1.45 if we neglect the 1 = O space-scales. These values are larger than the average value of 1.25 found by Bazell and Désert in an analysis of three cirrus maps. However, there was variation within each of several images they analyzed (see their figure *2)* with a maximum value of D = 1.40 for plate 2. Dickman et al.'s study of 100 μm maps of molecular regions also found $D \approx 1.25$, similar to those found for cirrus clouds. Whereas the cloud B5 studied with CO maps (Langer *et al.* 1993) has D ranging from 1.3 to 1.7.

However, the strong dependence of D on area (Figure 12) shows that these maps are multifractal with D ranging from 1.1 to 1.8, and can not be characterized by a single scale. Chappell and Scalo (1993) also concluded that the cirrus maps of several regions were multifractal. In general D increases with area reaching values about 1.8. This dependence suggests that the smallest features are regular objects, probably determined by the pixelization (discreteness) inherent in the maps, but that the majority of features obey a scaling law for turbulence (but not necessarily Kolmogorov turbulence), while the largest features at L_1 and L_0 are filamentary-like structures. Visual inspection shows these largest features consist of long single filaments and web-like structures. The latter are likely due to the overlap of separate clouds along the line-of-sight which appear as one object in projection due to the lack of velocity information in the IRAS maps. Further analysis of the turbulent nature of the maps is limited by the lack of this velocity information. What we need are hydrodynamical model calculations which can produce scaling laws for comparison to the observations. However, within the limitations of the data the dynamics of the gas does not appear to be dominated by either gravity or ordered magnetic fields. Our results suggest~~s~~ that the forces that control the structure at large and small scales in the cirrus map are different. We do not find this surprising considering the very large range of scales and objects contained in the IRAS maps.

In conclusion, we have explored the question of whether multiscale transforms can be used to provide statistical and global measures of astronomical emission maps, and whether they can be used to distinguish maps. We found that the Laplacian Pyramid Transform provides an amplitude space that can be used to distinguish maps and characterize their properties. The development of such computational, tools is important for the analysis of the very large body of spatial and spatial-spectral data bases that are becoming available with current radio and infrared survey instruments. More work remains to be done to derive connections between the various map measures and the underlying dynamical forces. We expect to extend this line of analysis to other types of maps and to regions evolving under different forces and energy sources.

Acknowledgments

We would like to thank Dr. N. Gautier of JPL for many useful discussions regarding power spectra and for providing the original IRAS images. RWW wishes to thank JPL for hospitality during time spent as Distinguished Visiting Scientist while working on this project. This research was conducted at the Jet Propulsion Laboratory, California Institute of Technology under contract with the National Aeronautics and Space Administration and with support from the LTSA and ADP programs.

REFERENCES

Abergel, A., Boulanger, F., Delouis, J. M., Dudziak, G., and Steindling, S. 1995, A & A in press.

Adams, F. C. 1992, ApJ, 387,572.

Adams, F. C. and Wisernan, J. J. 1994, Ap J, 435,693.

Anderson, C. H. and Rakshit, S. 1994, *Interpolation in Multiscale Representations*, in *Shape in Picture: Mathematical Description of Shape in Groy-Scale Images, Ed.* Ying-Lie, NATO ASI Series F: Computer and Systems Sciences, Vol. 126, pp291 -301 (Springer-Verlag, Berlin).

Auriere, M. and Coupinot, G. 1989, *Proc. of the 1st ESO/ST-ECF Data Analysis Workshop,* eds. Grobs et al.

Bazell, D. and Désert, F. X. 1988, ApJ, 333, 353.

Burt, P. J. and Adelson, E. H. 1984, IEEE Trans. Commun., vol. COM-31, 532.

Burt, P. J., Anderson, C. H., Siniger, J. O., and van der Wal, G. 1986, NATO ASI series, Vol. F25, p 133, *Pyramidal Systems for Computer Vision,* Eds. V. Cantoni and S. Levialdi (Springer-Verlag: Heidelberg).

Chappell, D. and Scalo, J 1993, *Multi-Fractal Column Density Scaling in Local Star-Forming Complexes,* preprint.

Coupinot, G., Hecquet, J., Auriere, M., and Fautaully, R. 1992, A&A, 259, 701.

Daubechies, 1. 1992, *Ten Lectures on Wavelets,* CBMS-NSF Regional Conference Series in Applied Mathematics (Philadelphia: SIAM).

Dickman, R. L., Horvath, M A., and Margulis, M. 1990, ApJ, 365, 586.

Falgarone, E., Phillips, T. G., and Walker, C. K., 1991, ApJ, 378, 186.

Farge, M. 1992, Ann. Rev. Fluid Mech., 24, 395.

Farge, M., Holschneider, M, Colonna, J. F., 1990a, in *Topological Fluid Mechanics,* ed. H. K. Moffatt, pp. 765. Cambridge: Cambridge Univ. Press.

Farge, M., Guezennec, Y., Ho, C. M., Meneveau, C. 1990b, *Proc. Summer Prog. Cent. Turbulence Res.,* Stanford Univ., NASA-Ames.

Gill, A. G. and Henriksen, R. N. 1990, ApJ Letters, 365, L27.

Green, D. A. 1993, MNRAS, 262, 327.

Grossman, A. and Morlet, J. 1987, *Mathematics and Physics, Lectures on Recent Results*, ed. 1... Streit (World Scientific).

Houlahan, P. and Scale, J. 1990, ApJ Suppl., 72, 133 and 1992, ApJ, 393, 172.

Kleiner, S. C. and Dickman, R. L. 1984, ApJ, 286, 255 and 1985, ApJ, 295,466.

Kleiner, S. C. and Dickman, R. L. 1987, ApJ, 312, 837.

Langer, W. D., Wilson, R. W., Goldsmith, P. F., and Beichman, C. A. 1989, ApJ, 337, 355.

Langer, W. D., Wilson, R. W., and Anderson, C. H. 1993, ApJ Letters, 408, 1.45.

Langer, W. D., Wilson, R. W., Anderson, C. H., and Castets, A. 1995, *2nd Zermatt Conference on the Physics and Chemistry of Clouds* held in Zermatt, Switzerland September 1993, Eds. J. Stutzki and G. Winnewisser, Springer Verlag, in press 1995.

Martinez, V. J., Paredes, S., and Saar, E., 1993, MNRAS, 260, 365.

Press, W. H., Flannery, B. P., Teukolosky, S. A., and Vetterling, W. T. 1993, *Numerical Recipes 2nd Edition* (Cambridge University Press: Cambridge).

Rauzy, S., Lachièze-Rey, M., and Henriksen, R. N. 1993, A&A, 273, 357.

Simoncelli, E. P., Freeman, W. T., Adelson, E. H., and Heeger, D. J., 1992, IEEE Trans., Info. Theory, Special Issue on Wavelets, 38, 587.

Slezak, E., Bijaoui, A., and Mars, G. 1990, A&A, 227, 301.

Stutzki, J. and Gusten, R. 1990, ApJ, 356, 513.

Strang, G. T. 1989, SIAM Review, 31, 614-627.

Van der Wal, G. S. 1991, The Sarnoff Pyramid Chip, *Proc. Computer Architecture for Machine Perception, (CAMP-9* 1), Paris, p. 69.

Wickerhauser, M. V. 1994, “Adaptive Wavelet Analysis from Theory to Software”, (A. K. Peters: Wellesley, MA)

Williams, J. P. and Blitz, L. 1993, Ap. J. Letters, 405, L75.

Williams, J. P., de Geus, E., and Blitz, L. 1994, ApJ, 428, 693.

Wiseman, J. J. and Adams, F. C. 1994, ApJ, 435, 708.

Figure Captions

Figure 1. Scale invariant filter bank. Filter responses, F_n(k)= F_0(2^n k), are plotted on the left. Typical filtered signals are drawn on top of the appropriate sampling intervals in the figure.

Figure 2a Contour plot of the 100 micron image of the Chameleon region (map centered at DEC(1950) = 12h and RA(1950) = -800), where the axis are in arcmin with respect to the center. Intensity contours range from 2 x 10^6 to 1.48 x 10^8 Jy Sr^{-1} in increments of 2 x 10^6.

Figure 2b Contour plot of the 100 micron image of the North Polar region (map centered at DEC = 90^{o}, RA = 0^h and RA goes counterclockwise with 6^h on the left), where the axis are in arcmin with respect to the center. Intensity contours range from 1.5 x 10^6 to 1.65 x 10^7 Jy Sr^{-1} in increments of 1.5 x 10^6.

Figure 3a. Gray scale images of GO, the original map, and the Laplacian amplitude maps L_0, L_1, and L_2 of the Chameleon region (clockwise starting from upper left). In the Laplacian maps the light and dark regions are positive and negative amplitudes, respectively.

Figure 3b. Gray scale images of GO, the original map, and the Laplacian amplitude maps L_0, L_1, and L_2 of the North Polar region (clockwise starting from upper left). In the Laplacian maps the light and dark regions are positive and negative amplitudes, respectively.

Figure 3c. Comparison of the $l = 1$ Laplacian amplitude map (left panel) for Chameleon with the corresponding space-scale amplitude map for a wavelet transform using the Daubechies wavelet four transform (right panel). The wavelet Daubechies map (in gray scale) shows less correspondence with physical structure than the Laplacian

Pyramid Transform with the original map. While both transform can be used to reconstruct the original map to very high accuracy their utility for identifying structural components is different. The number scale along the axes label the pixels.

Figure 4a Space-scale energy density maps L_0, L_1, L_2, and L_3 for the Chameleon region in color.

Figure 4b Space-scale energy density maps L_0, L_1, L_2, and L_3 for the North Pole region in color.

Figure 5 Global energy (power) spectrum for three maps, Chameleon and North Pole 100 µm emission, and Perseus ^{13}CO emission, and a random image (top panel). For comparison all power spectrum have been normalized to one at l = O. The bottom panel shows only the three astronomical images in order to make it easier to see differences in the dependence with 1.

Figure 6 The number of distinct features isolated in the energy density maps as a function of space-scale. Two plots are shown for each region, one for all features in the maps and the other for all features with area greater than 15 arcmin^2, the resolution of the IRAS beam at 100 pm. The North Pole region is dominated by small scale features, with area less than 15 arcmin^2, which are probably due to noise.

Figure 7 Average intensity versus area for positive amplitude features extracted from the LPT transform maps for all space-scales combined, $\sum_{l=0}^{5} L_l$. A log– log fit to these data is shown in the panels.

Figure 8 The local energy E is plotted versus area and shows the tendency for the larger features to have a higher energy density. Fits to log E -- *log A* are given in each panel.

Figure 9 Histograms of the area, intensity, local energy, and average intensity, <1>, of each of the positive amplitude features extracted from the LPT transform maps combined for all space-scales, $\sum_{l=0}^{5} L_n$.

Figure 10. Plot of log P versus *log A* for features in the 1 = 1 and *1* = 2 space-scale maps for the Chameleon and North Pole regions, These plots indicate that D is a function of area and is multi-fractal. Also shown in the figures are linear and quadratic fits, where it can be seen that the latter gives a much better fit to the data.

Figure 11 Hausdorff dimension, D, versus space-scale derived from a linear fit to log P – *log A,* using the entire range in area for features in the energy density maps. D can be considered an average value for each of the maps. For both regions D has the same general behavior with space-scale.

Figure 12 The Hausdorff dimension, D, derived from a polynomial fit to log P – log A is plotted as a function of area A for features extracted from three energy density space-scale maps in the Chameleon and North Pole regions. These plots show that D is multi-fractal in both cloud regions.

Figure 13 Number of features N versus Hausdorff dimension D for features extracted from the energy density maps for three space-scales.

Figure 14 The average intermittence for each feature in four space-scale maps for the Chameleon and North Pole regions. This measure can be used to categorize and identify features in the maps, for example galaxies have. large (L) at small areas, while noise or small diffuse features have very low values of $(\imath \rangle$.

Figure 15 Histograms of the area, intensity, and local energy of positive amplitude features extracted from the LPT transform maps of Chameleon and North Pole regions for space-scales l = 1 and 1 =4.

Figure 6 Fraction of power contained in features with positive amplitude to total power as a function of 1 for Chameleon and North Pole regions.

Figure 7 Number of features as a function of intensity I for all of the amplitude maps combined. Fits to a $\log \mathrm{N} - \log I$ are given separately for the behavior at small and large areas. These curves are, to first approximation, proportional to the mass distribution of fragments in the maps.

Figure 18 Number of features versus local energy for all the features extracted from the energy density maps. Fits to $\log N - \log E$ are given in the panels.

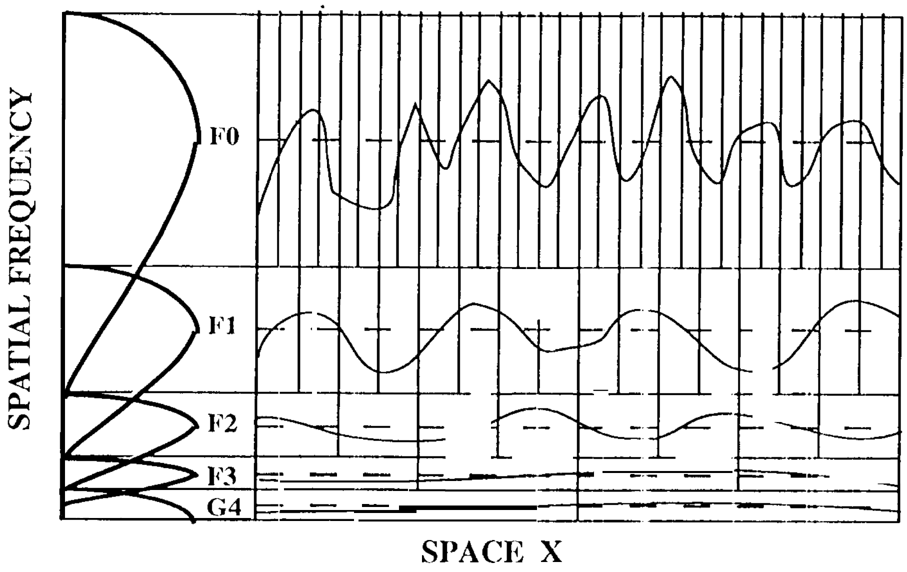

Figure 1

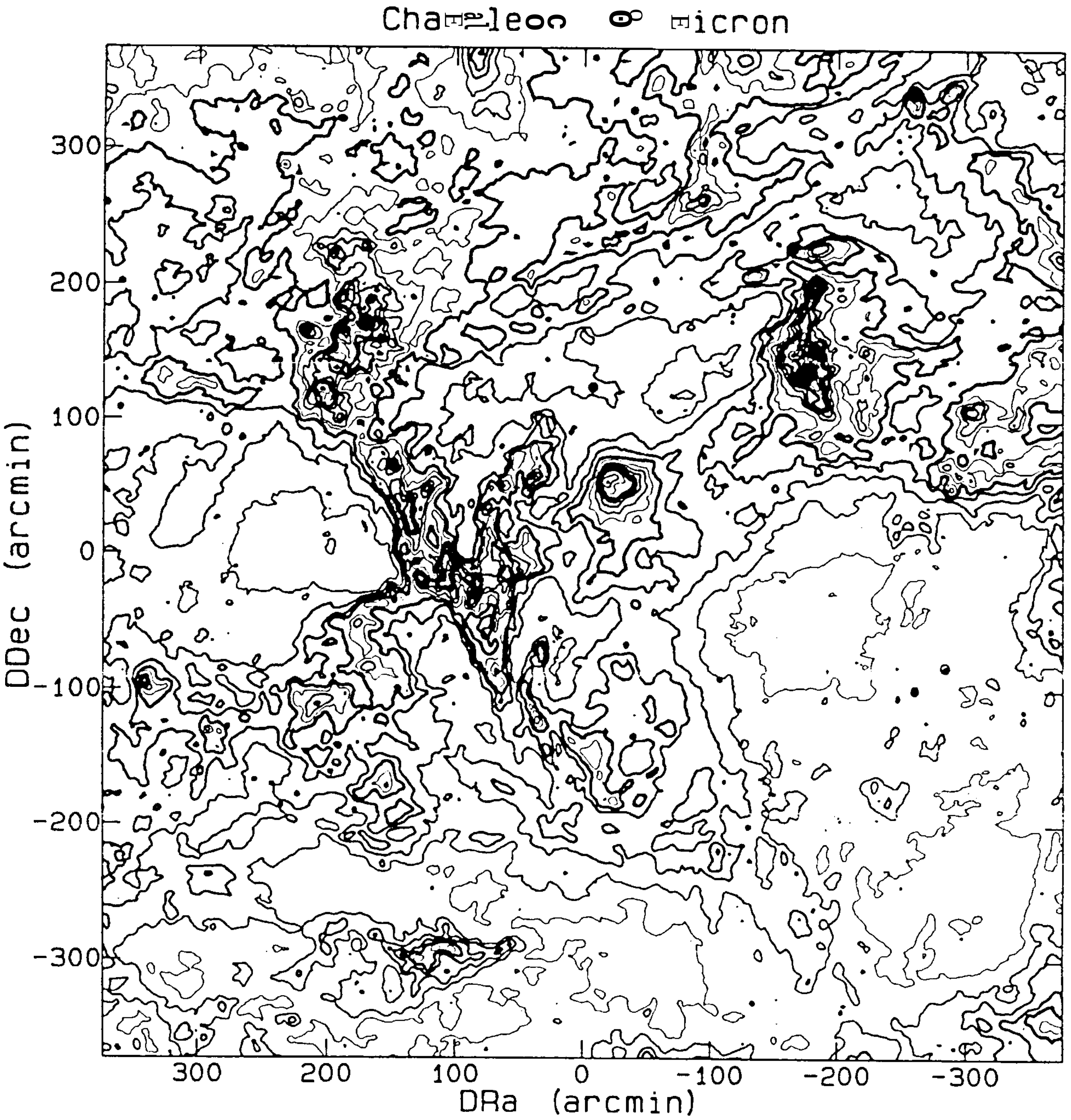

Figure 2a

2e+06. 4e+06. 1.48e+08

Figure 2b

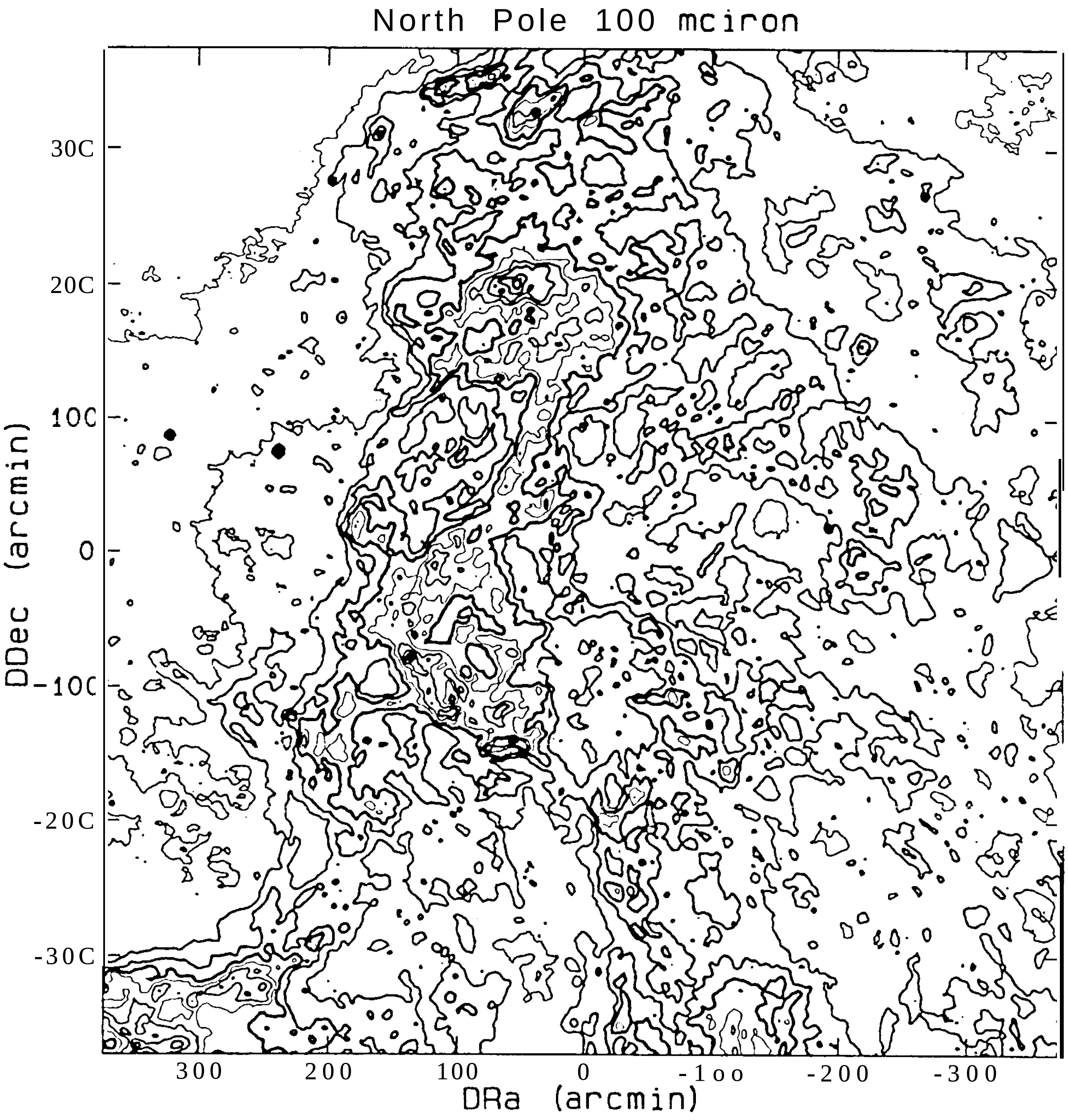
North Pole 100 mciron
DDec (arcmin)
30C
20C
10C
0
-10C
-20C
-30C
DRa (arcmin)
300
200
100
0
-1oo
-200
-300
1.5e+06, 3e+06, . . . 1.65e+07

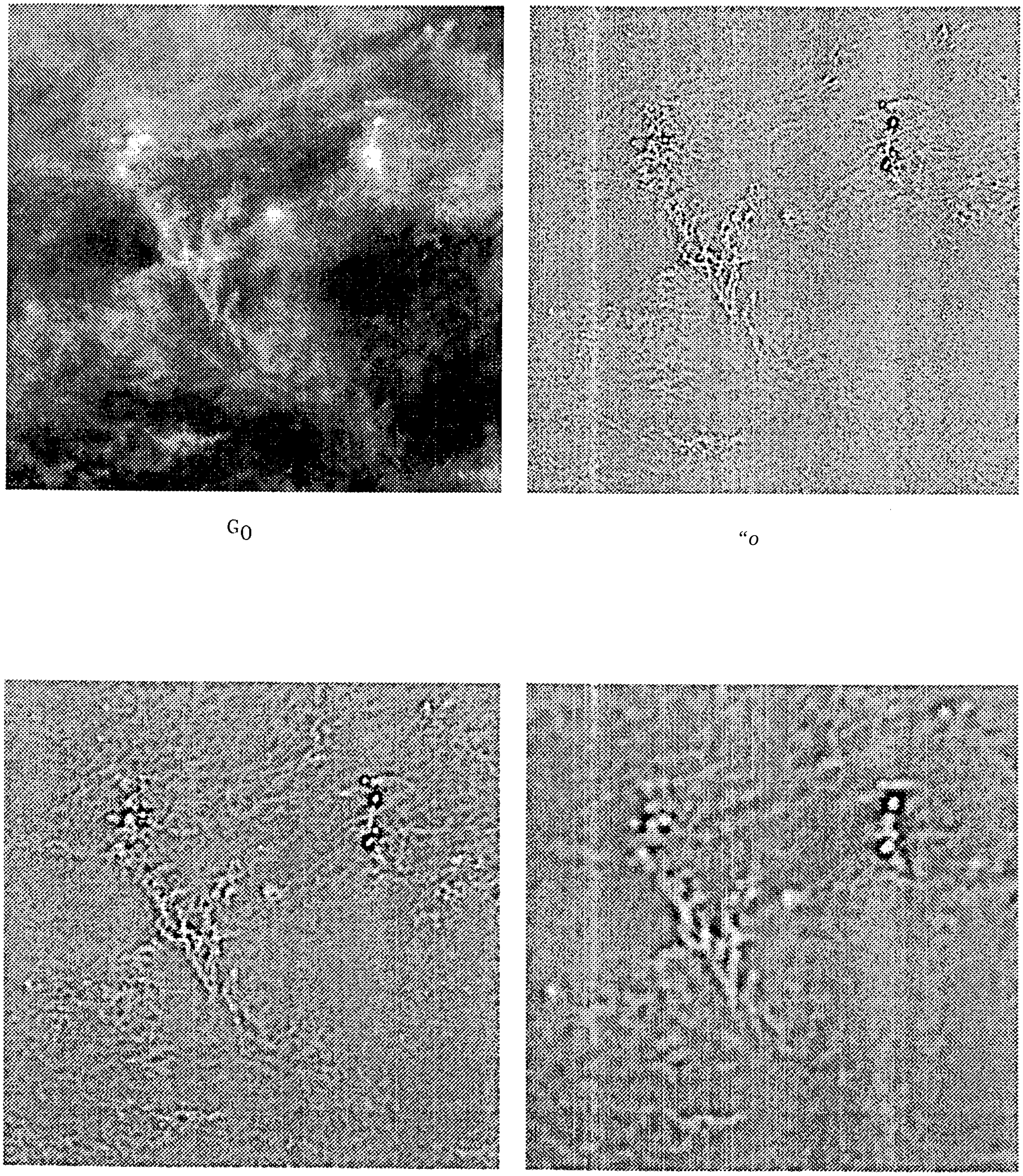

G_0

“o

L_1

L_2

Figure 3a

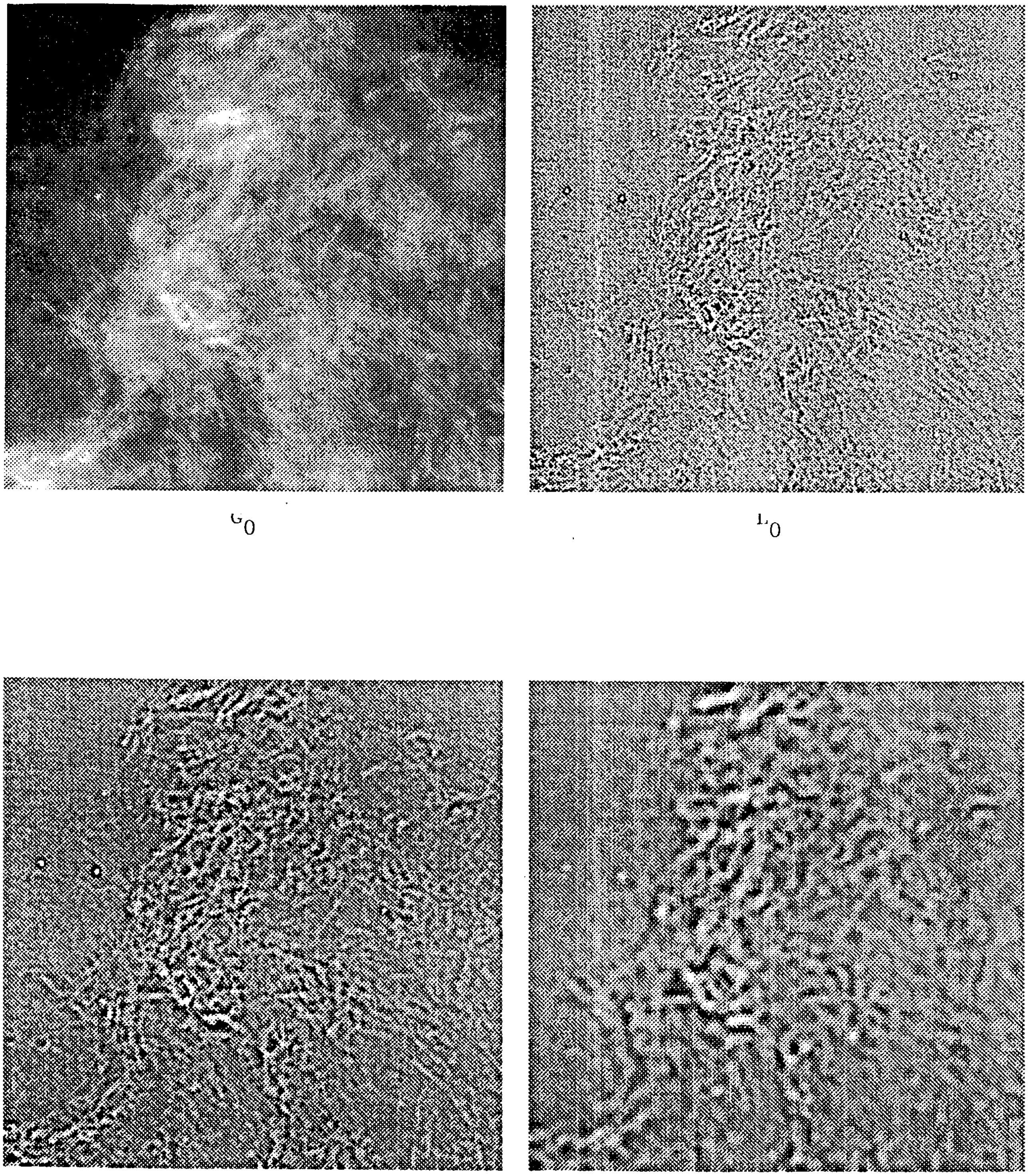

G_0 L_0

L_1 L_2

Figure 3b

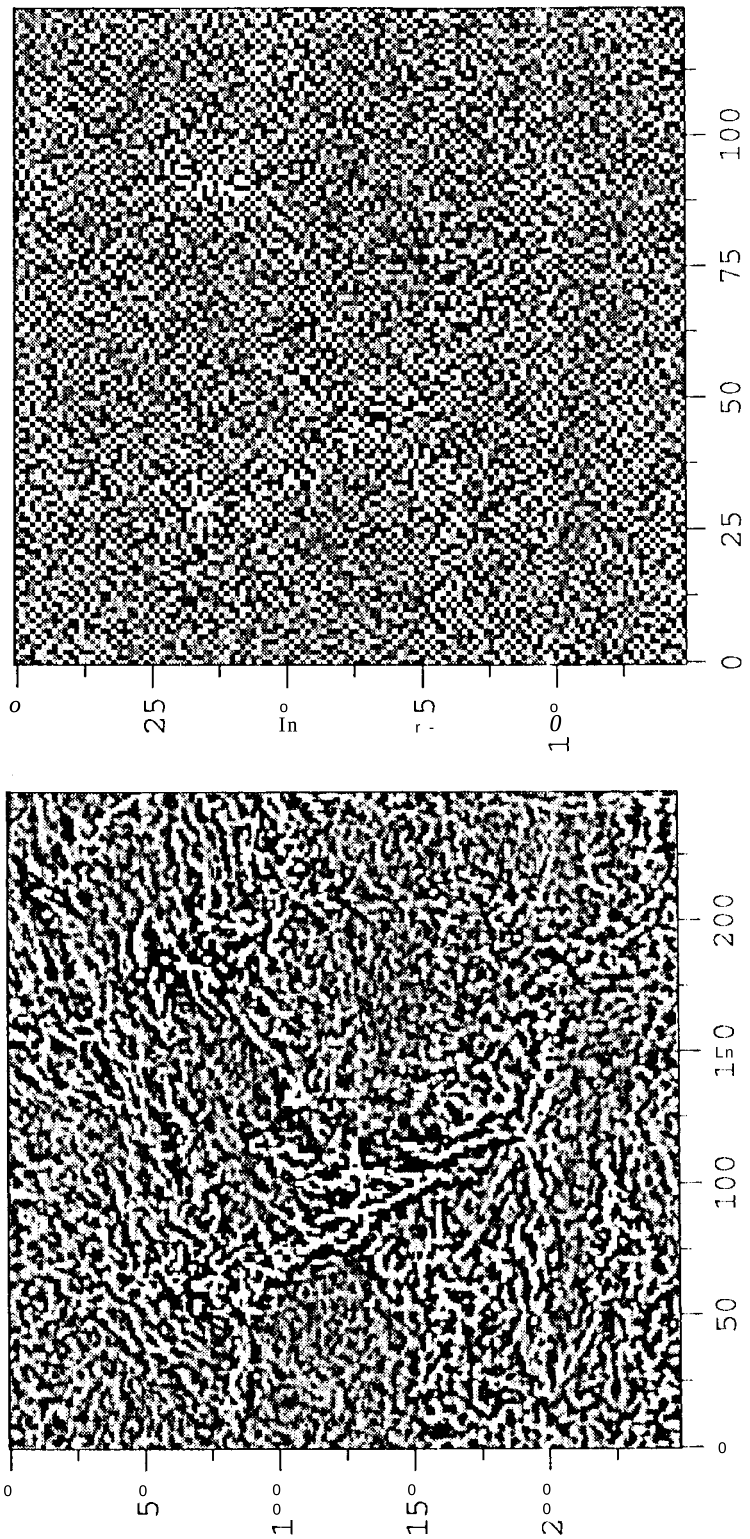

Figure 3c

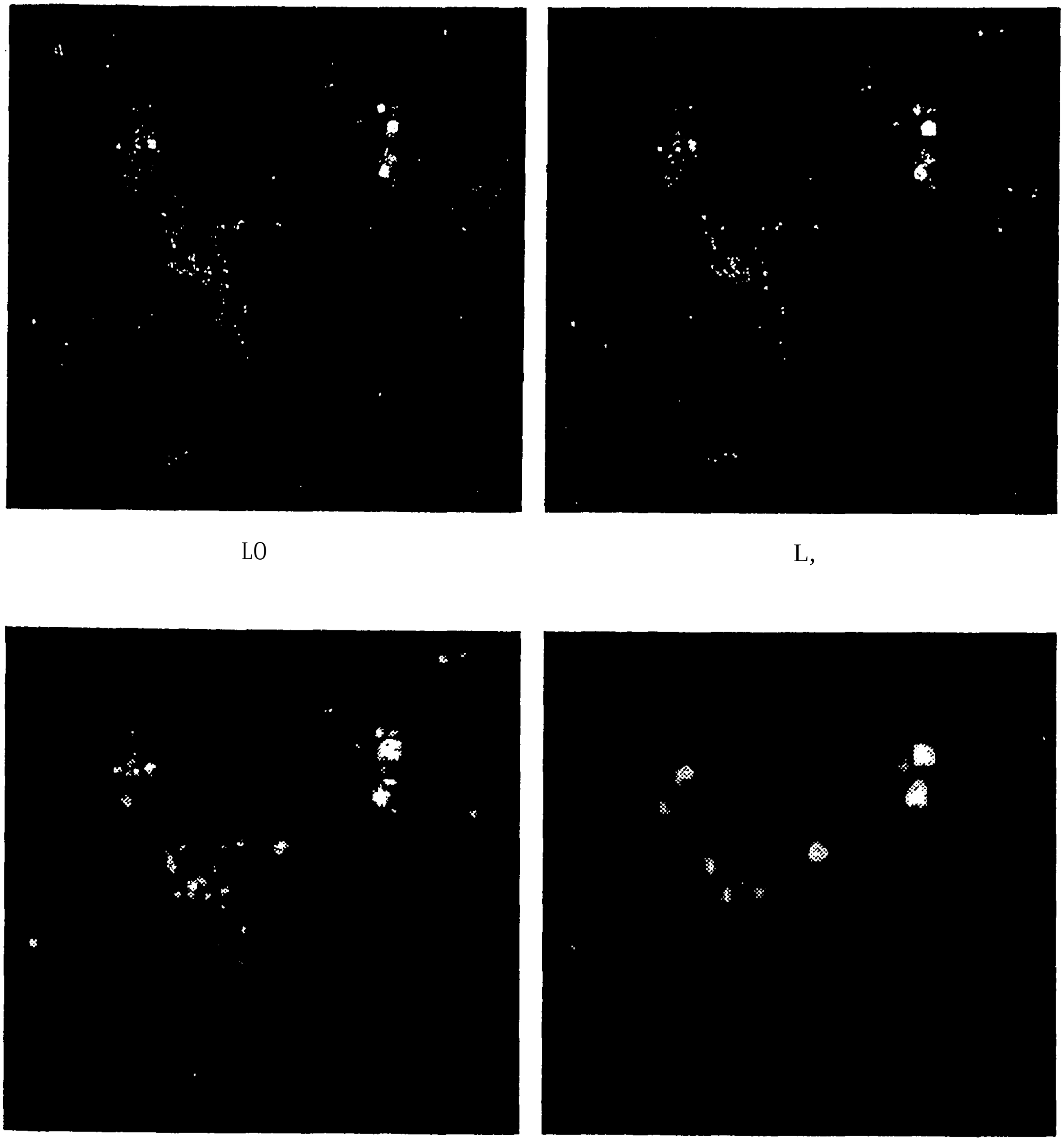

LO

L,

L_2

L_3

Fig. 3a. Chameleon power, wavelet amplitude squared 1234567'89012345 12345678901234567890 01234567890123456789 01234567890123456789 01234

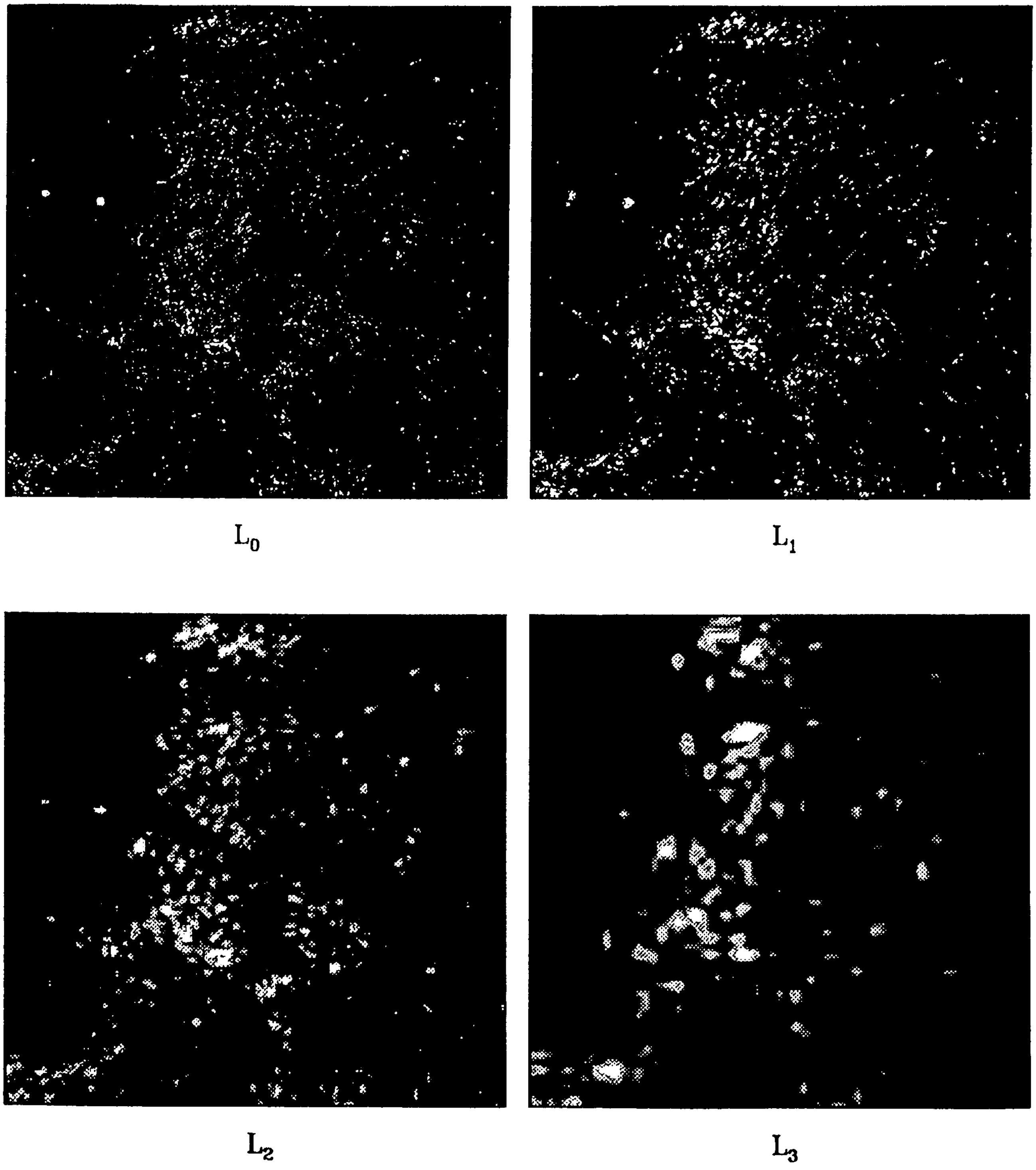

L_0 L_1

L_2 L_3

Fig. 3a. Polar power, wavelet amplitude squared 12345678901234567890 12345678901234567890l 2345678901234567 []90123456789012345678 90 1234

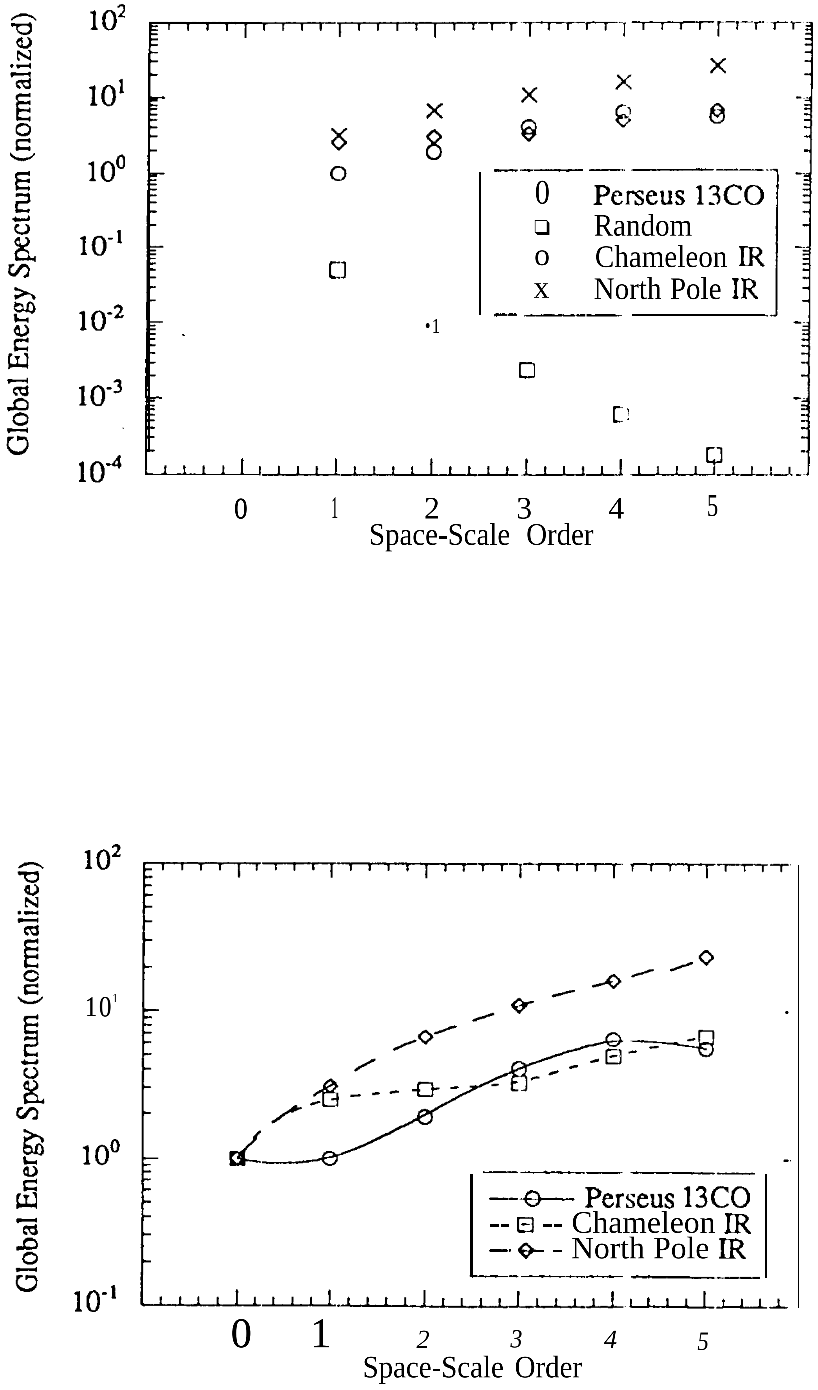
Global Energy Spectrum (normalized)
10^2
10^1
10^0
10^{-1}
10^{-2}
10^{-3}
10^{-4}
0 Perseus 13CO
❑ Random
o Chameleon IR
x North Pole IR
0
1
2
3
4
5
Space-Scale Order
Global Energy Spectrum (normalized)
10^2
10^1
10^0
10^{-1}
Perseus 13CO
Chameleon IR
North Pole IR
0
1
2
3
4
5
Space-Scale Order

Figure 5

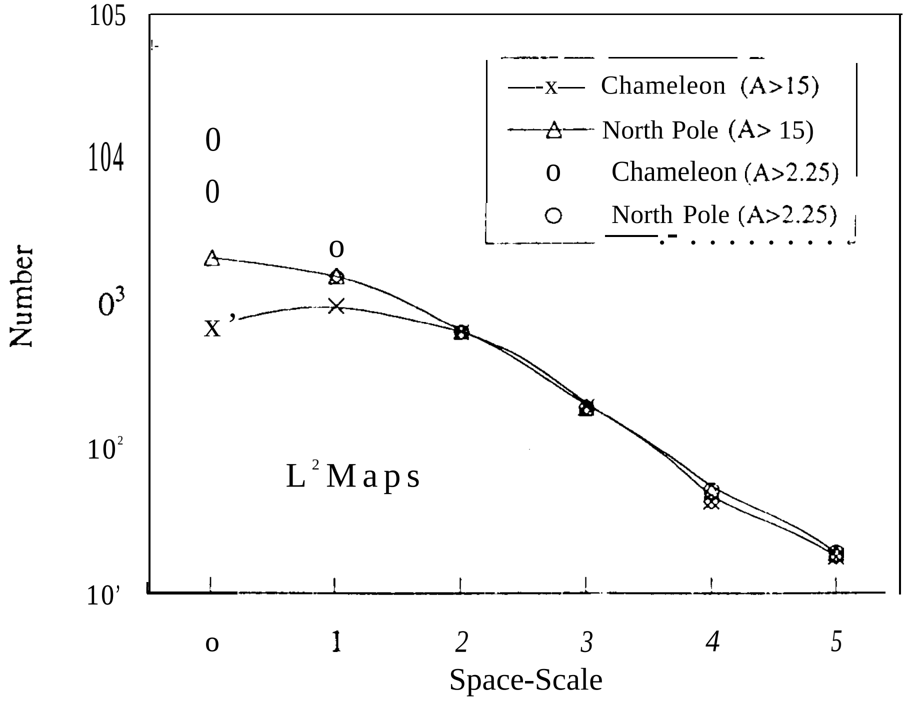
105
104
0³
10²
10'
Number
—x— Chameleon (A>15)
—Δ— North Pole (A> 15)
o Chameleon (A>2.25)
○ North Pole (A>2.25)
L² Maps
o
1
2
3
4
5
Space-Scale

Figure 6

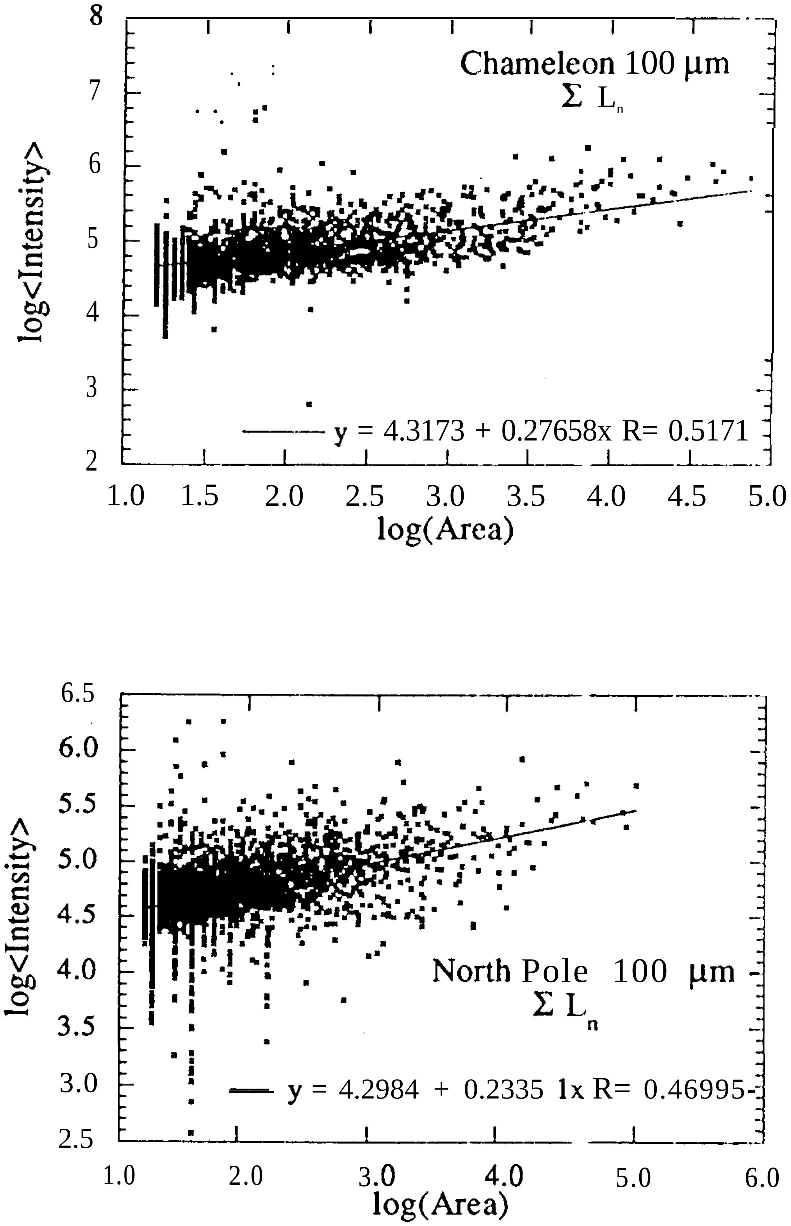
Chameleon 100 μm
Σ L$_n$
y = 4.3173 + 0.27658x R= 0.5171
log<Intensity>
8
7
6
5
4
3
2
1.0
1.5
2.0
2.5
3.0
3.5
4.0
4.5
5.0
log(Area)
North Pole 100 μm
Σ L$_n$
y = 4.2984 + 0.2335 1x R= 0.46995
log<Intensity>
6.5
6.0
5.5
5.0
4.5
4.0
3.5
3.0
2.5
1.0
2.0
3.0
4.0
5.0
6.0
log(Area)

Figure 7

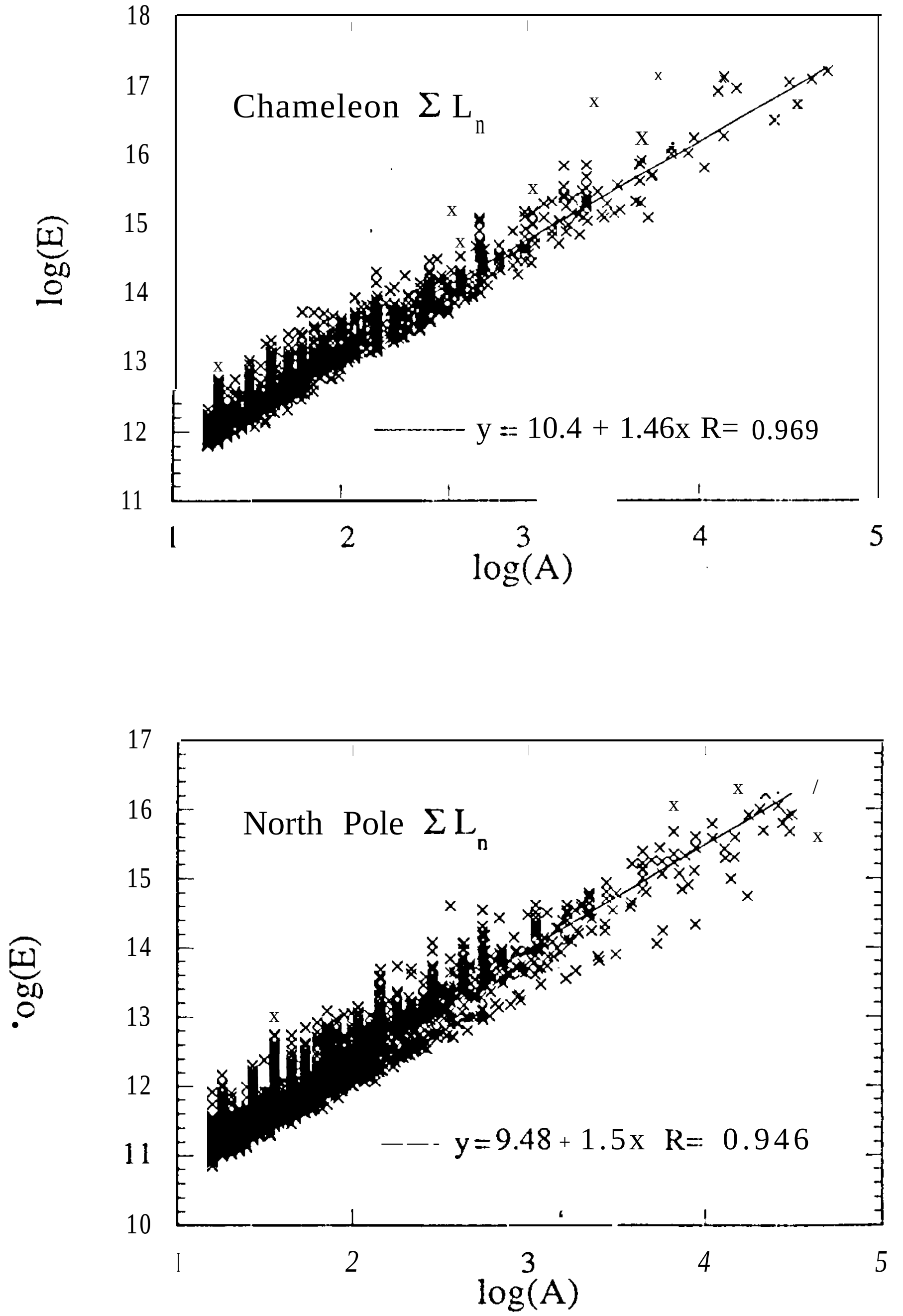
Chameleon Σ L$_n$
y = 10.4 + 1.46x R= 0.969
log(E)
log(A)
18
17
16
15
14
13
12
11
1
2
3
4
5
North Pole Σ L$_n$
y=9.48 + 1.5x R= 0.946
log(E)
log(A)
17
16
15
14
13
12
11
10
1
2
3
4
5

Figure 8

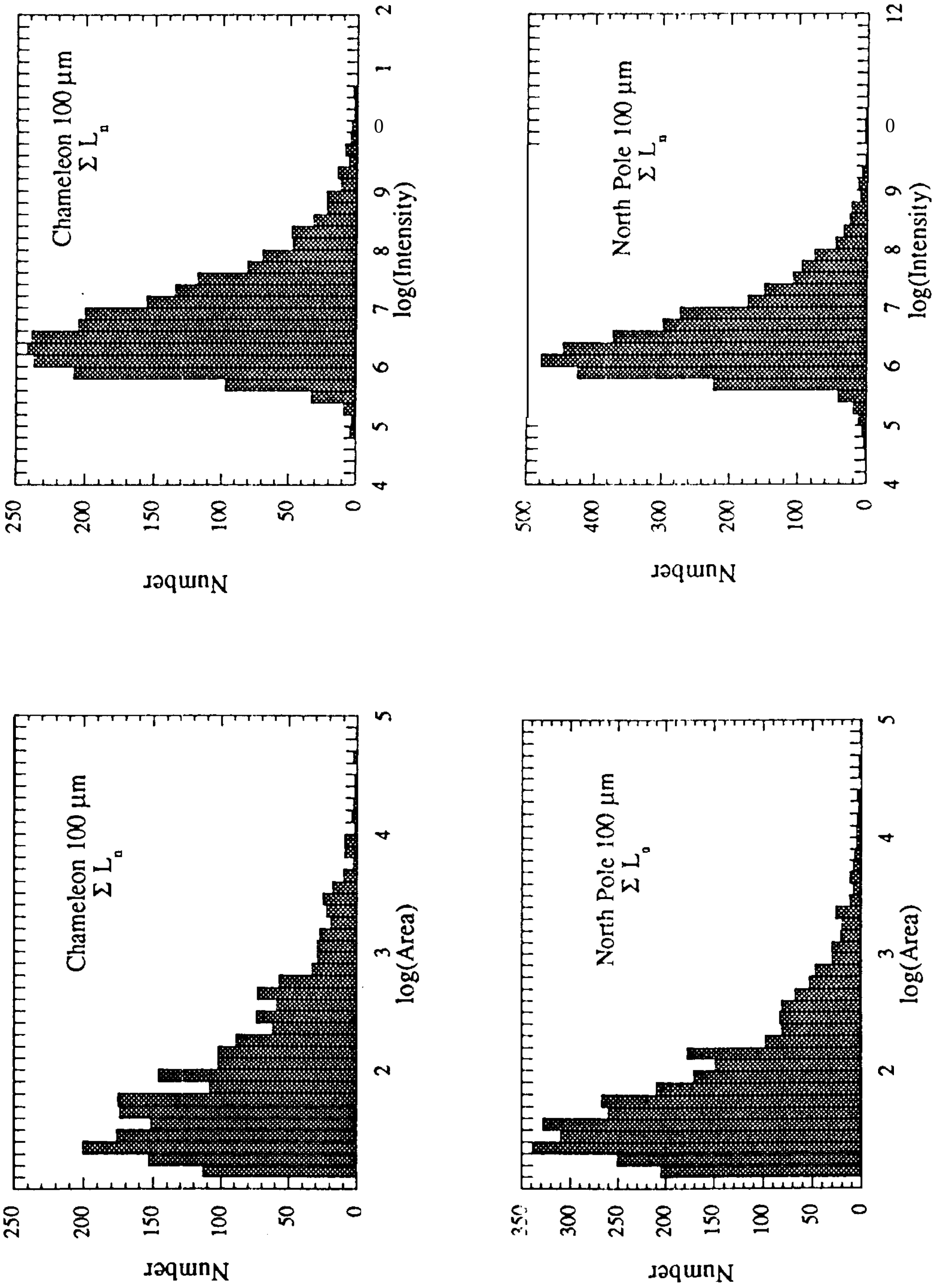
Chameleon 100 µm
Σ Lα
North Pole 100 µm
Σ Lα
Number
log(Area)
log(Intensity)
0
50
100
150
200
250
300
350
400
500
2
3
4
5
6
7
8
9
0
1
12

Figure 9a

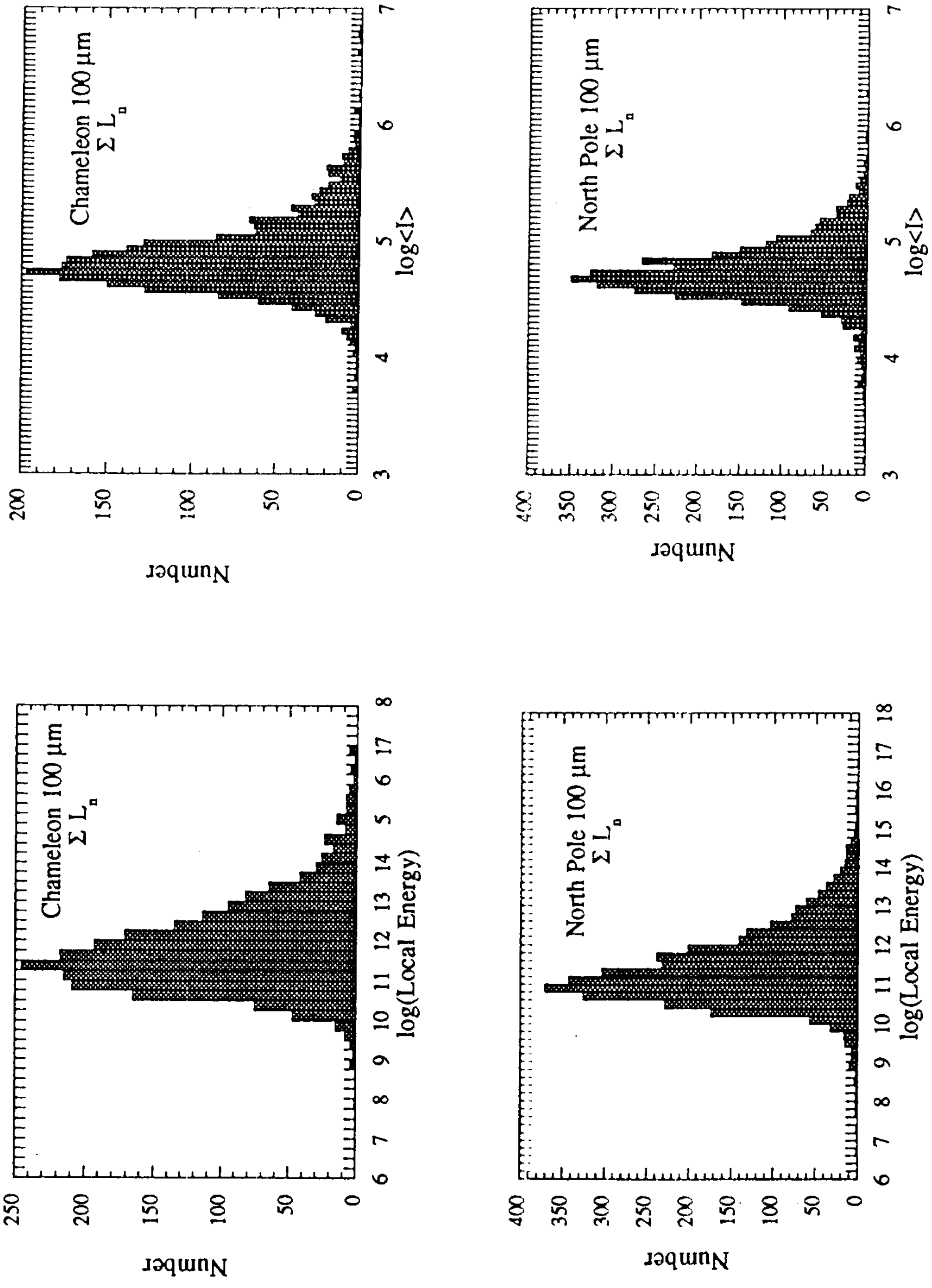
Chameleon 100 µm
Σ L_n
North Pole 100 µm
Σ L_n
Number
log(Local Energy)
log<I>
0
50
100
150
200
250
300
350
400
3
4
5
6
7
8
9
10
11
12
13
14
15
16
17
18

Figure 9b

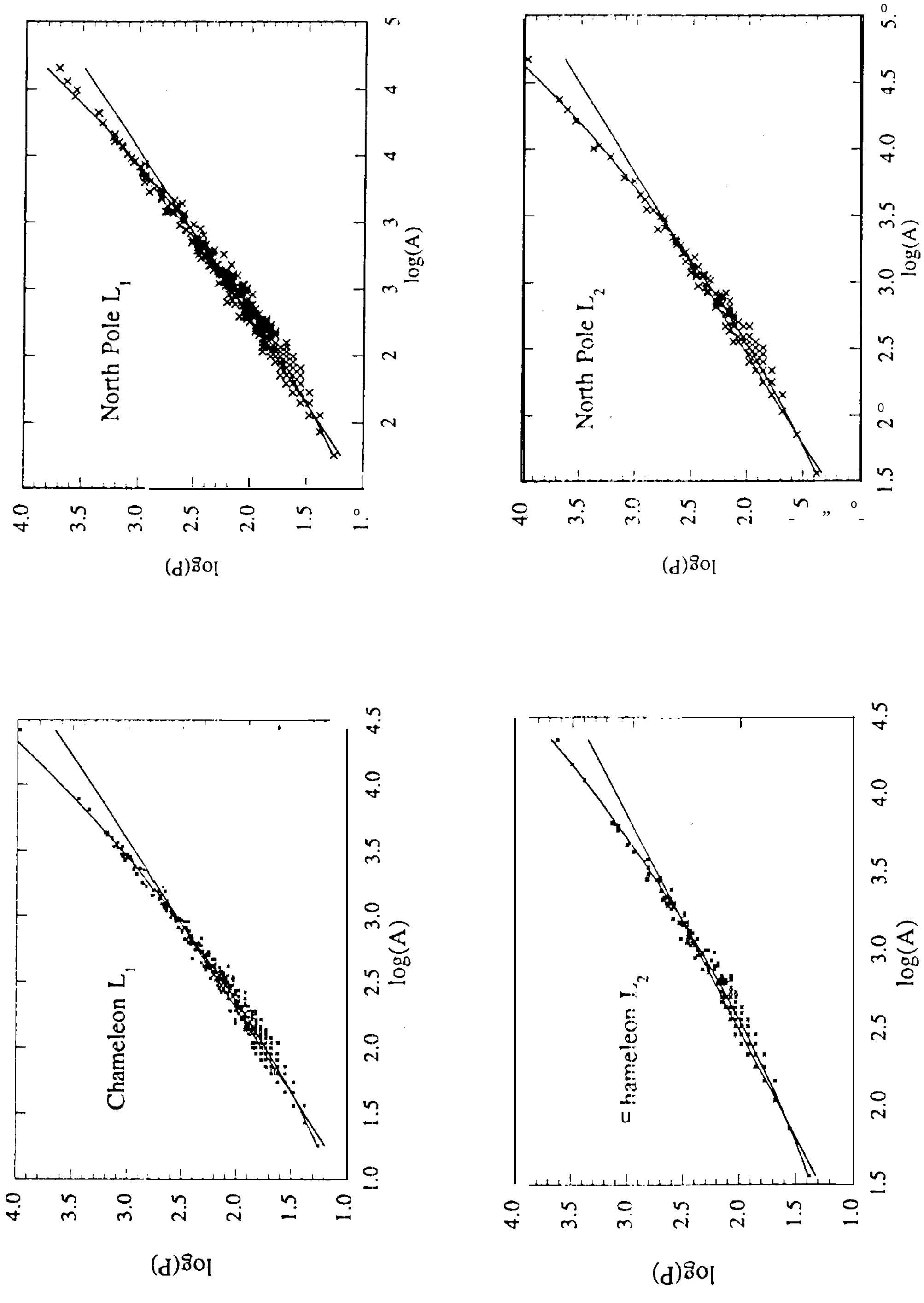
North Pole L$_1$
North Pole L$_2$
Chameleon L$_1$
Chameleon L$_2$
log(A)
log(P)
1.0
1.5
2.0
2.5
3.0
3.5
4.0
4.5
5

Figure 10

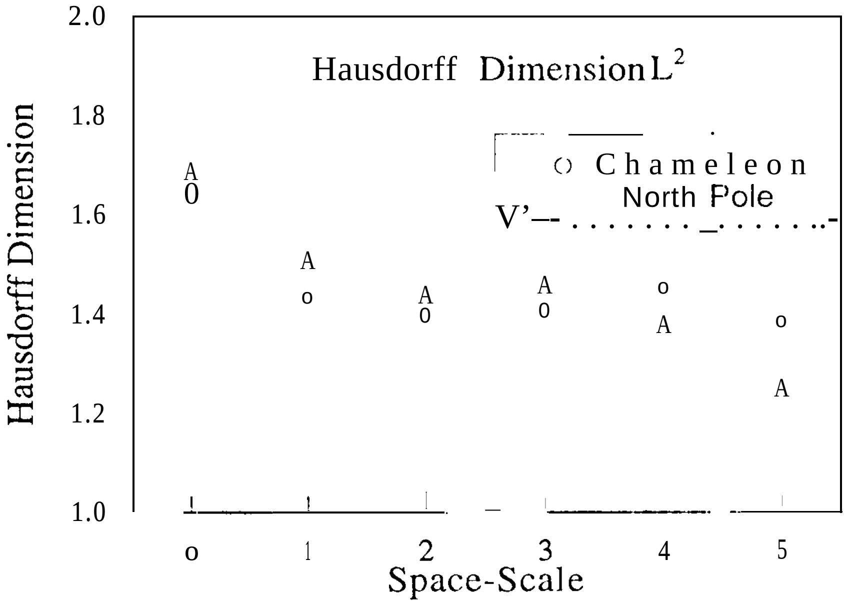
Hausdorff Dimension L2
Chameleon
North Pole
Hausdorff Dimension
2.0
1.8
1.6
1.4
1.2
1.0
0
1
2
3
4
5
Space-Scale

Figure 11

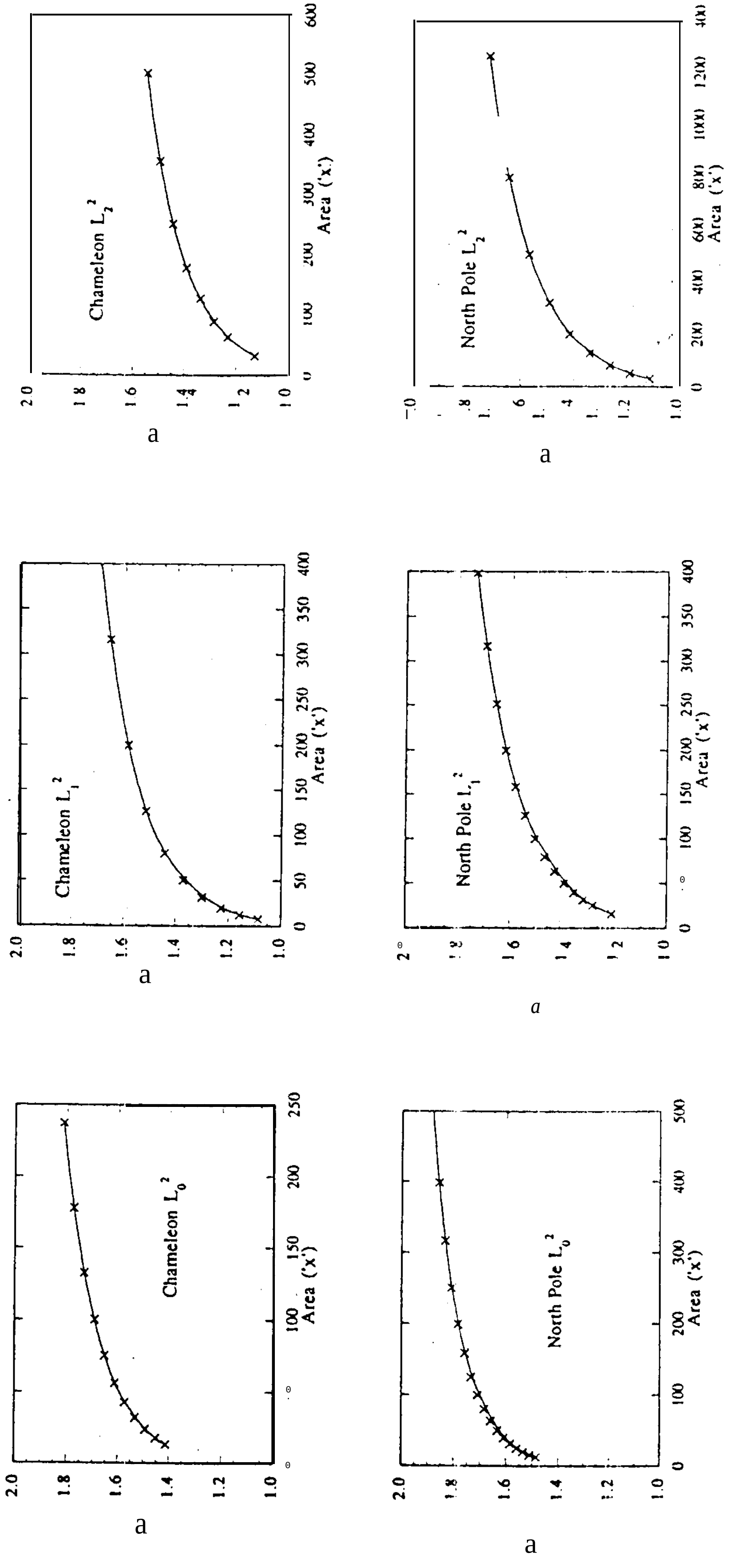
Chameleon L_0^2
Chameleon L_1^2
Chameleon L_2^2
North Pole L_0^2
North Pole L_1^2
North Pole L_2^2
Area ('x')
a
2.0
1.8
1.6
1.4
1.2
1.0
0
50
100
150
200
250
300
350
400
500
600
800
1000
1200

Figure 12

Figure 13

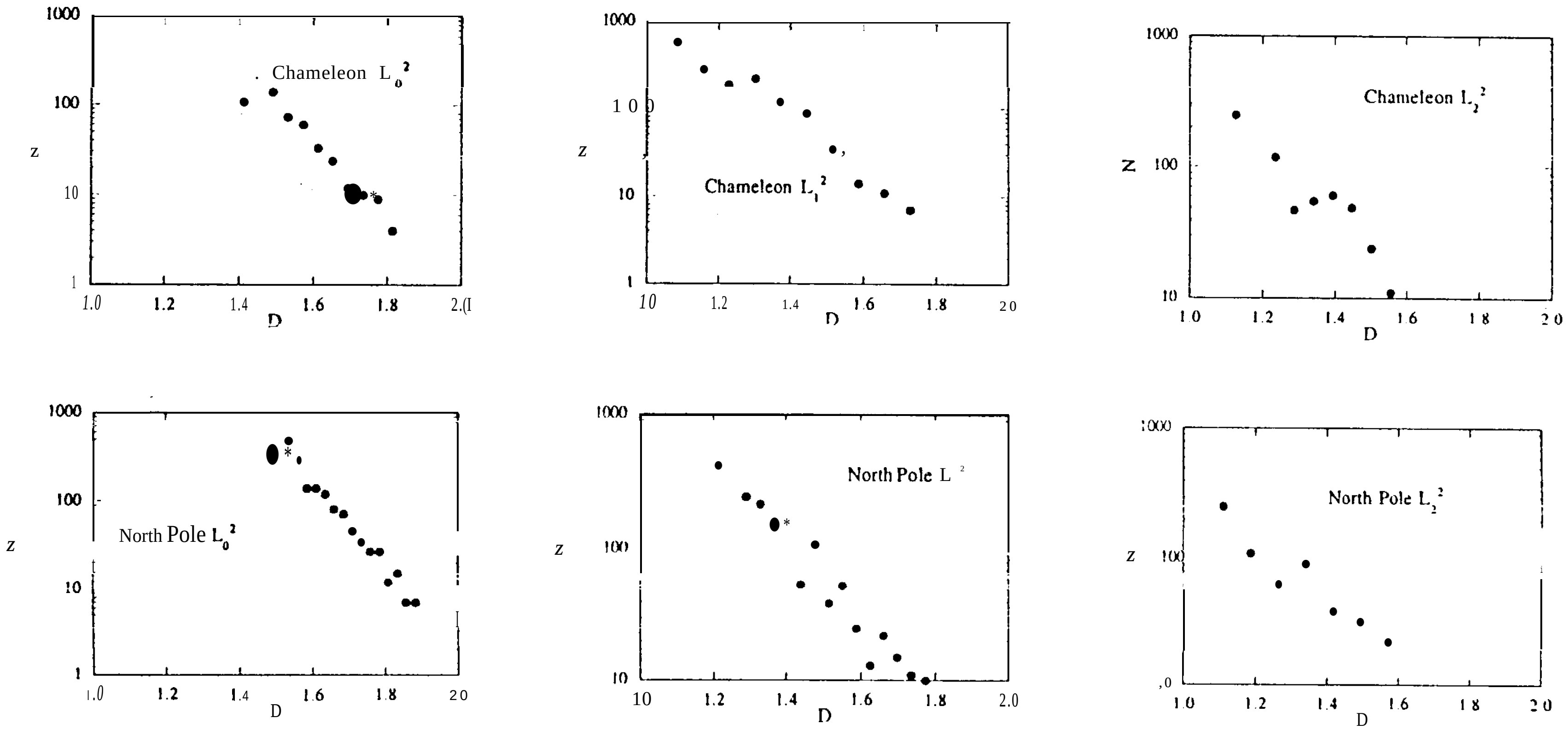

Chameleon L_0^2
Chameleon L_1^2
Chameleon L_2^2
North Pole L_0^2
North Pole L^2
North Pole L_2^2
z
N
D
1000
100
10
1
1.0
1.2
1.4
1.6
1.8
2.0

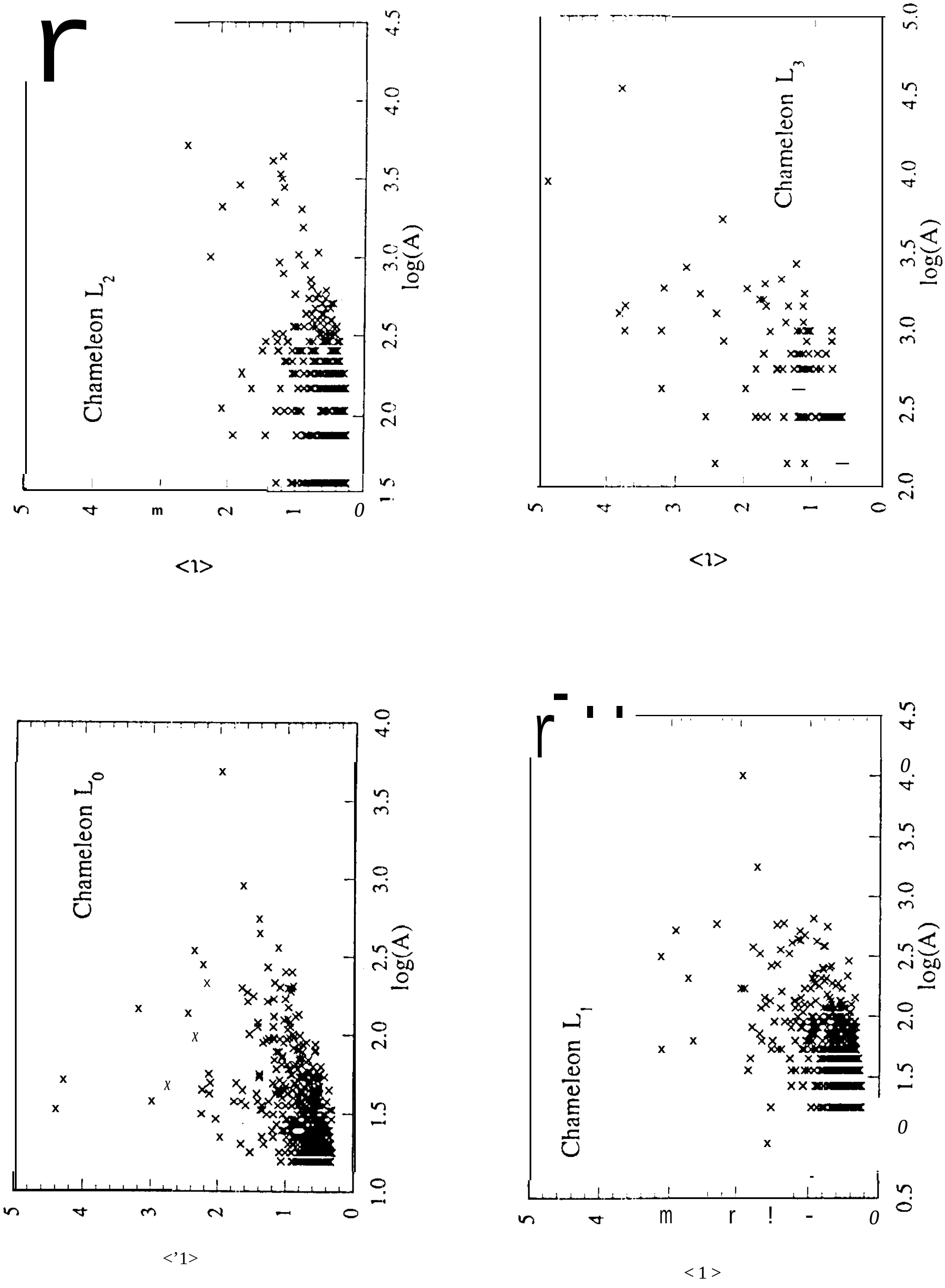
Chameleon L_0
Chameleon L_1
Chameleon L_2
Chameleon L_3
log(A)
<1>
0
1
2
3
4
5
1.0
1.5
2.0
2.5
3.0
3.5
4.0
4.5
5.0
0.5

Figure 14a

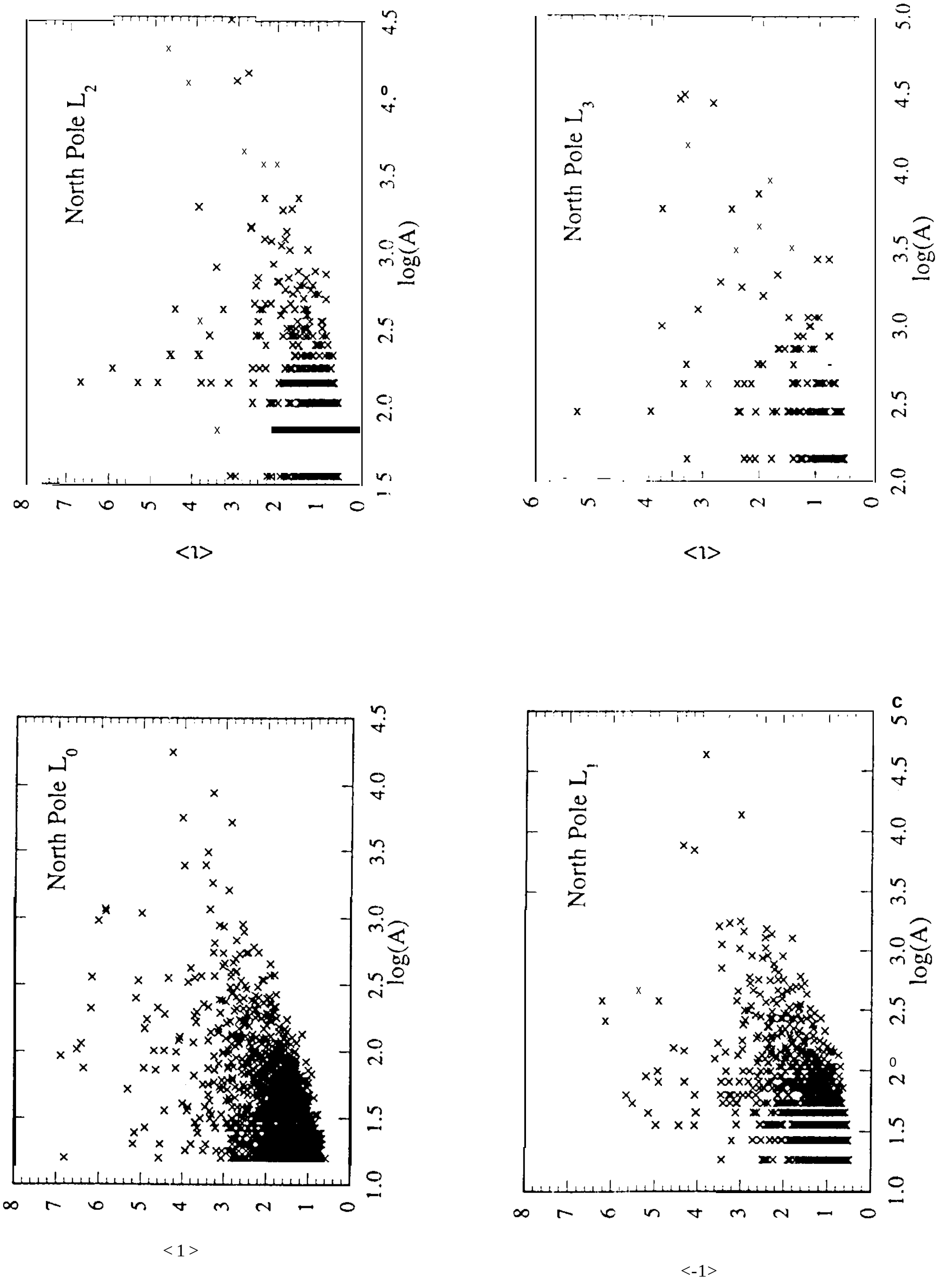
North Pole L_0
North Pole L_1
North Pole L_2
North Pole L_3
log(A)
log(A)
log(A)
log(A)
<1>
<-1>
<1>
<1>
1.0 1.5 2.0 2.5 3.0 3.5 4.0 4.5
1.0 1.5 2.0 2.5 3.0 3.5 4.0 4.5 5.0
1.5 2.0 2.5 3.0 3.5 4.0 4.5
2.0 2.5 3.0 3.5 4.0 4.5 5.0
0 1 2 3 4 5 6 7 8
0 1 2 3 4 5 6

Figure 14b

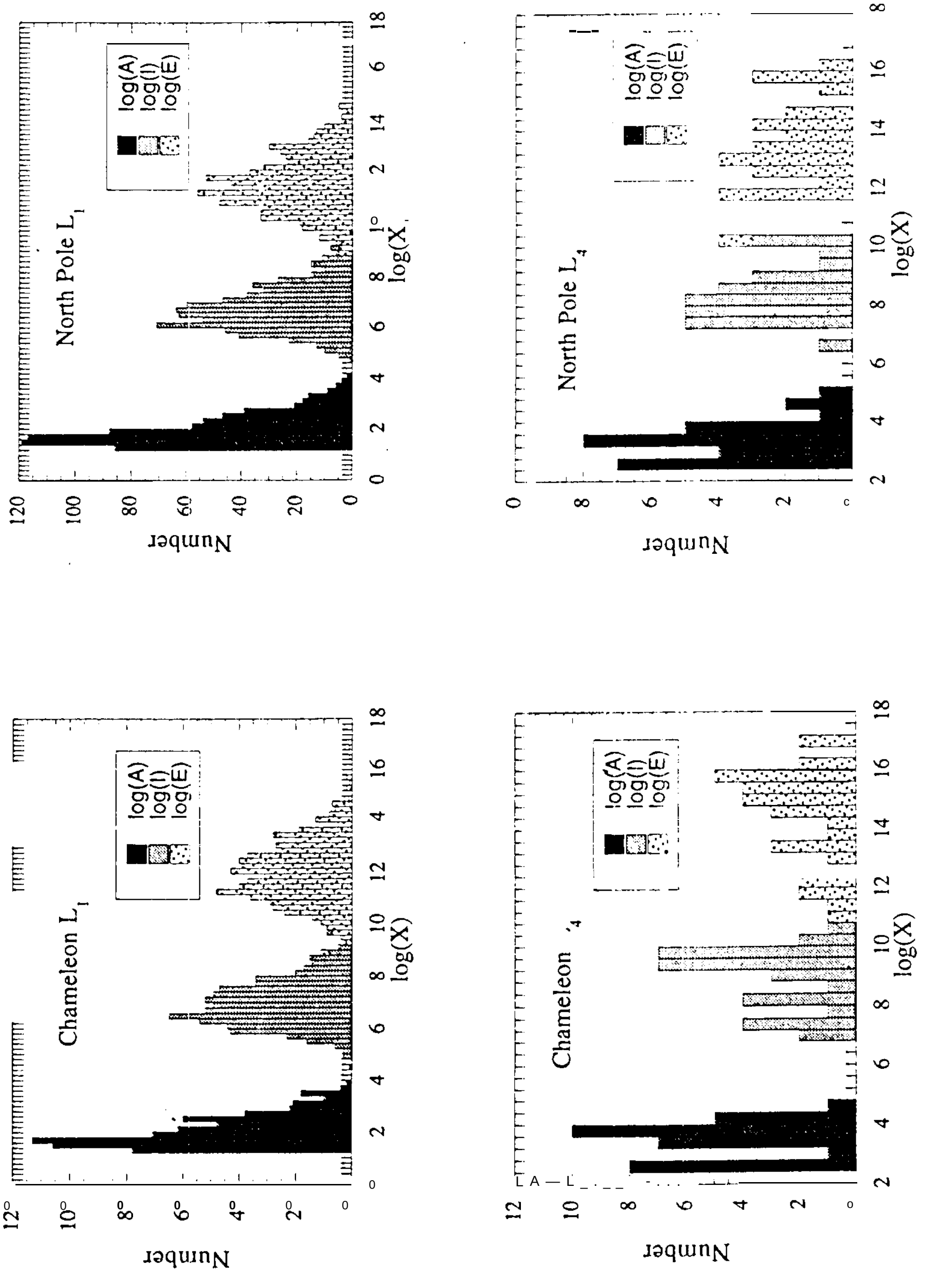
Chameleon L1
North Pole L1
Chameleon L4
North Pole L4
log(A)
log(I)
log(E)
Number
log(X)
0
2
4
6
8
10
12
14
16
18
20
40
60
80
100
120

Figure 15

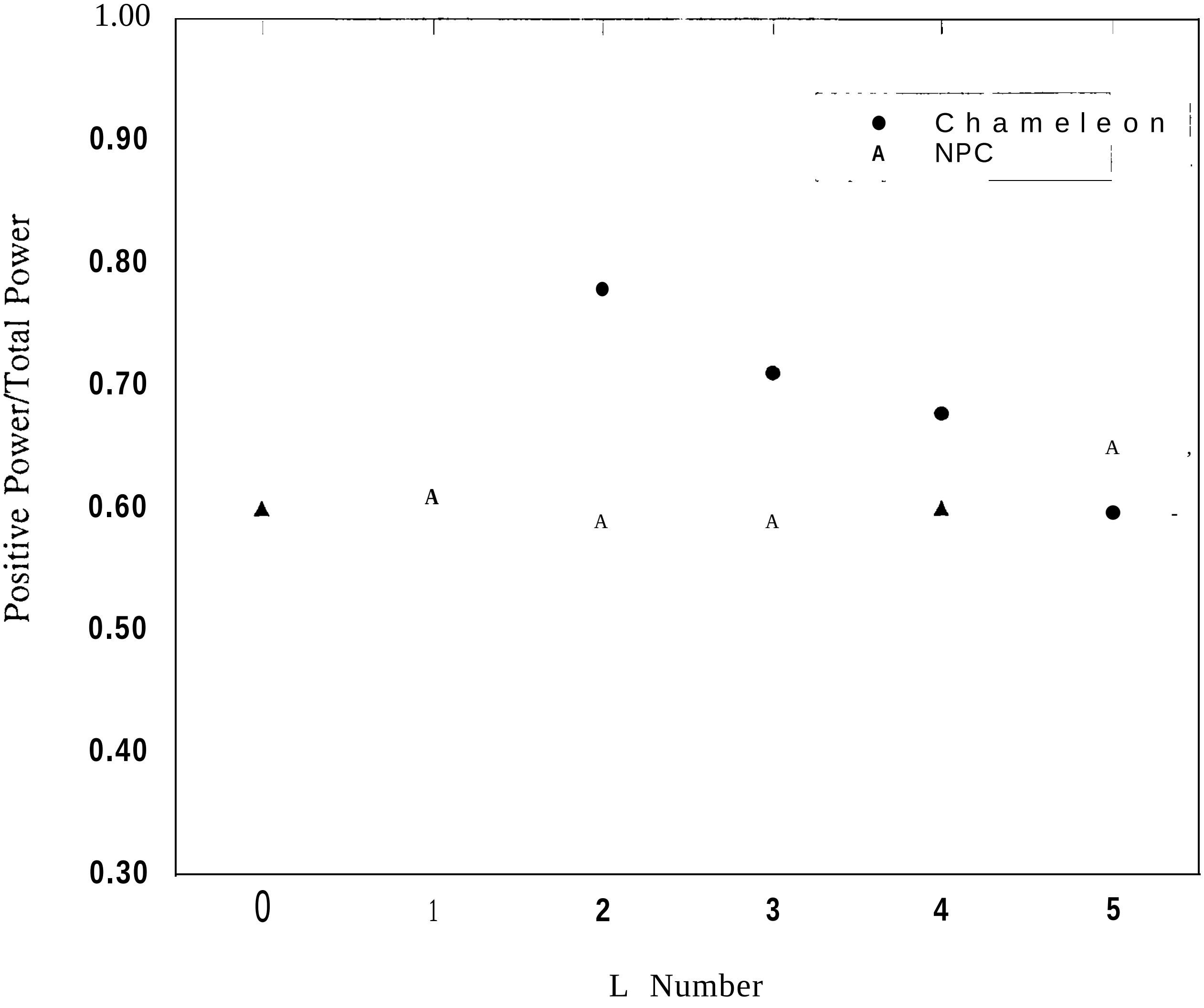
1.00
0.90
0.80
0.70
0.60
0.50
0.40
0.30
Positive Power/Total Power
● Chameleon
▲ NPC
0
1
2
3
4
5
L Number

Figure 16 .

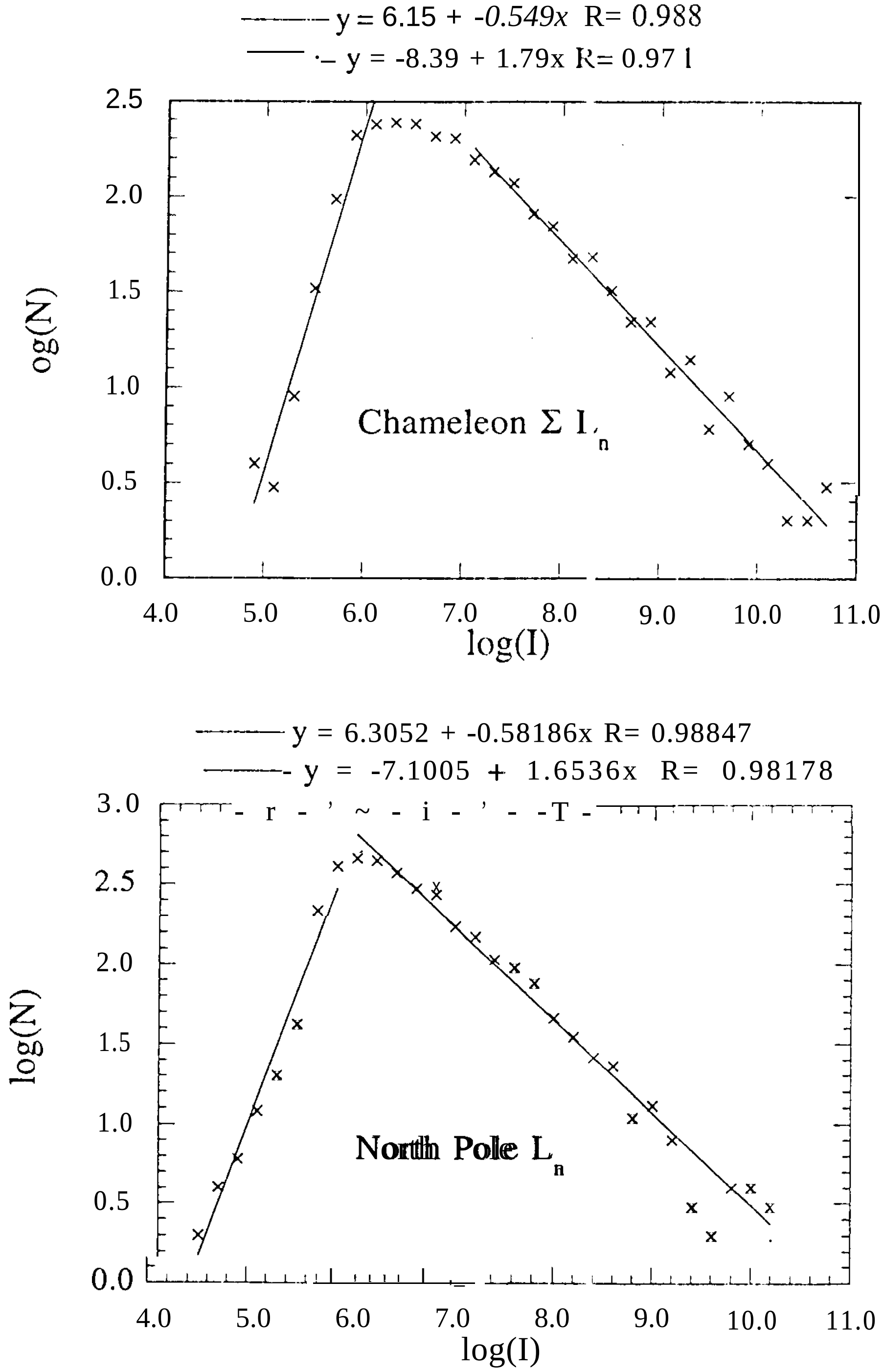
y = 6.15 + -0.549x R= 0.988
y = -8.39 + 1.79x R= 0.971
2.5
2.0
1.5
1.0
0.5
0.0
og(N)
Chameleon Σ I_n
4.0
5.0
6.0
7.0
8.0
9.0
10.0
11.0
log(I)
y = 6.3052 + -0.58186x R= 0.98847
y = -7.1005 + 1.6536x R= 0.98178
3.0
2.5
2.0
1.5
1.0
0.5
0.0
log(N)
North Pole L_n
4.0
5.0
6.0
7.0
8.0
9.0
10.0
11.0
log(I)

Figure 17

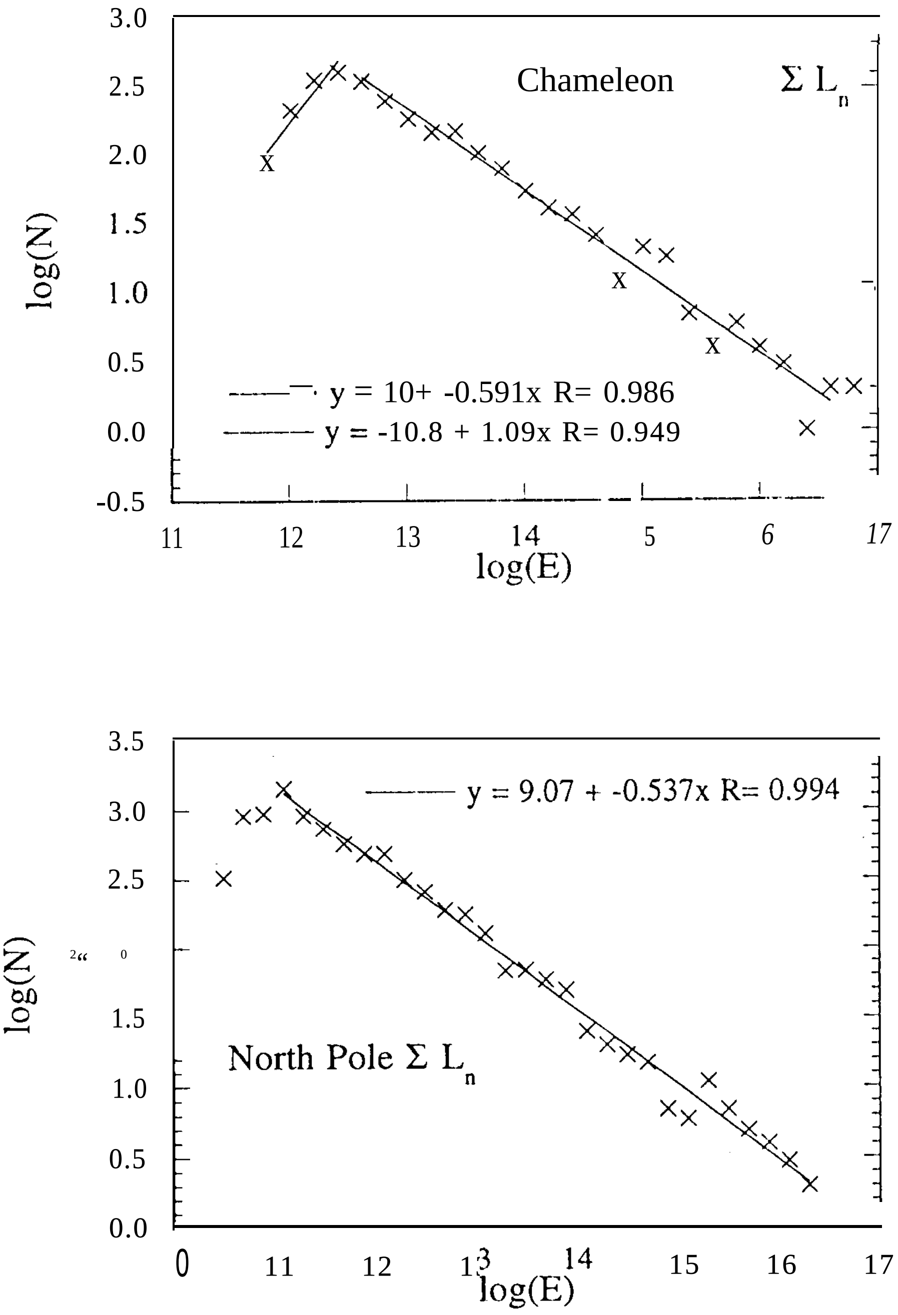
3.0
2.5
2.0
1.5
1.0
0.5
0.0
-0.5
log(N)
Chameleon
Σ L_n
y = 10+ -0.591x R= 0.986
y = -10.8 + 1.09x R= 0.949
11
12
13
14
5
6
17
log(E)
3.5
3.0
2.5
1.5
1.0
0.5
0.0
log(N)
y = 9.07 + -0.537x R= 0.994
North Pole Σ L_n
0
11
12
13
14
15
16
17
log(E)

Figure 18